Wrocław University of Technology
Centre of Advanced Materials and Nanotechnology

# Materials Science
# **Poland**

Vol.22 • No. 1 • 2004

Oficyna Wydawnicza Politechniki Wrocławskiej

**Materials Science** is an interdisciplinary journal devoted to experimental and theoretical research into the synthesis, structure, properties and applications of materials.

**Among the materials of interest are:**

- glasses and ceramics
- sol-gel materials
- photoactive materials (including materials for nonlinear optics)
- laser materials
- photonic crystals
- semiconductor micro- and nanostructures
- piezo-, pyro- and ferroelectric materials
- high-$T_c$, superconductors
- magnetic materials
- molecular materials (including polymers) for use in electronics and photonics
- novel solid phases
- other novel and unconventional materials

The broad spectrum of the areas of interest reflects the interdisciplinary nature of materials research. Papers covering the modelling of materials, their synthesis and characterisation, physicochemical aspects of their fabrication, properties and applications are welcome. In addition to regular papers, the journal features issues containing conference papers, as well as special issues on key topics in materials science.

Materials Science is published under the auspices of the Centre of Advanced Materials and Nanotechnology of the Wrocław University of Technology, in collaboration with the Institute of Low Temperatures and Structural Research of the Polish Academy of Sciences and the Wroclaw University of Economics.

All accepted papers are placed on the Web page of the journal and are available at the address: http://MaterialsScience.pwr.wroc.pl

**Editor-in-Chief**

Juliusz Sworakowski

Institute of Physical and Theoretical Chemistry
Wrocław University of Technology
Wybrzeże Wyspiańskiego 27
50-370 Wrocław, Poland
sworakowski@pwr.wroc.pl

Associate **Editors**

Wiesław Stręk

Institute of Low Temperature
and Structure Research
Polish Academy of Sciences
P.O.Box 1410
50-950 Wrocław 2, Poland
strek@int.pan.wroc.pl

Jerzy Hanuza

Department of Bioorganic Chemistry
Faculty of Industry and Economics
Wrocław University of Economics
Komandorska 118/120
53-345 Wrocław, Poland
hanuza@credit.ae.wroc.pl

**Scientific Secretary**

Krzysztof Maruszewski
Intitute of Materials Science and Applied Mechanics
Wrocław University of Technology
Wybrzeże Wyspiańskiego 27
50-370 Wrocław, Poland
maruszewski@pwr.wroc.pl

**Advisory Editorial Board**

Michel A. Aegerter, Saarbrücken, Germany
Ludwig J. Balk, Wuppertal, Germany
Victor E. Borisenko, Minsk, Belarus
Mikhaylo S. Brodyn, Kyiv, Ukraine
Maciej Bugajski, Warszawa, Poland
Alexander Bulinski, Ottawa, Canada
Roberto M. Faria, São Carlos, Brazil
Reimund Gerhard-Multhaupt, Potsdam, Germany
Paweł Hawrylak, Ottawa, Canada
Jorma Hölsä, Turku, Finland
Alexander A. Kaminskii, Moscow, Russia
Wacław Kasprzak, Wrocław, Poland
Andrzej Kłonkowski, Gdańsk, Poland
Seiji Kojima, Tsukuba, Japan
Shin-ya Koshihara, Tokyo, Japan
Marian Kryszewski, Łódź, Poland
Krzysztof J. Kurzydłowski, Warsaw, Poland
Jerzy M. Langer, Warsaw, Poland
Janina Legendziewicz, Wrocław, Poland
Benedykt Licznerski, Wrocław, Poland
Tadeusz Luty, Wrocław, Poland
Joop H. van der Maas, Utrecht, The Netherlands
Bolesław Mazurek, Wrocław, Poland
Gerd Meyer, Cologne, Germany
Jan Misiewicz, Wrocław, Poland
Jerzy Mroziński, Wrocław, Poland
Robert W. Munn, Manchester, U.K.
Krzysztof Nauka, Palo Alto, CA, U.S.A.
Stanislav Nešpůrek, Prague, Czech Republic
Romek Nowak, Santa Clara, CA, U.S.A.
Tetsuo Ogawa, Osaka, Japan
Renata Reisfeld, Jerusalem, Israel
Marek Samoć, Canberra, Australia
Jan Stankowski, Poznań, Poland
Leszek Stoch, Cracow, Poland
Jan van Turnhout, Delft, The Netherlands
Jacek Ulański, Łódź, Poland
Walter Wojciechowski, Wrocław, Poland
Vladislav Zolin, Moscow, Russia

The Journal is supported by the State Committee for Scientific Research

Editorial Office

Karol Langner
Łukasz Maciejewski

Printed in Poland

© Copyright by Oficyna Wydawnicza Politechniki Wrocławskiej, Wrocław 2004

Drukarnia Oficyny Wydawniczej Politechniki Wrocławskiej
Zam. nr 183/2004.

## Contents

M. Morita, D. Rau, S. Kajiyama, T. Sakurai, M. Baba, M. Iwamura, Luminescence properties of nanophosphors: metal ion-doped sol-gel silica glasses.....5
A. Stokłosa, J. Zajęcki, S.S. Kurek, Analysis of ionisation energies of ions, ionic radii in a crystal lattice and the energy of electrons in ionic cores of metal atoms.....17
A. Stokłosa, J. Zajęcki, S.S. Kurek, Effective nuclear charge of an ion.....35
O. P. Boiko, Ya. I. Vertsimakha, The kinetics of photoelectric processes near interfaces of $Co_{60}$/liquid crystals.....47
M.Z. Hussein, Z.B. Jubri, Z. Zainal, A.H. Yahya, Pamoate intercalated Zn-Al layered double hydroxide for the formation of layered organic-inorganic intercalate.....57
A. Kochel, Synthesis, structure and magnetic susceptibility of ammonium hexaiodorhenate(IV).... 69

*Materials Science-Poland*, *Vol. 22*, *No. 1*, *2004*

# Luminescence properties of nanophosphors: metal ion-doped sol-gel silica glasses*

M. MORITA[1**], D. RAU[1], S. KAJIYAMA[1], T. SAKURAI[1], M. BABA[2], M. IWAMURA[1]

[1]Department of Applied Chemistry, Seikei University, Kichijoji, Musashino-shi,Tokyo 180-8633, Japan

[2]ISSP, The University of Tokyo, Kashiwa 277-8581, Chiba, Japan

Photoluminescence of xerogel and sol-gel $SiO_2$ glasses doped with metal ions, metal complexes and semiconductor nanocrystals are investigated at 300 K and 10 K to clarify the optical properties and the electronic structures of nanophosphors. Sol-gel glasses doped with 3d, 4d and 5d transition metal ions exhibit a bright luminescence with various colours due to the $^3$LMCT transition associated with closed -shell molecular complex centres. Luminescence from rare earth(III) complexes doped in the same matrix serve as a sensitive probe to determine axial and chiral complex structures. Luminescence properties are investigated of doped semiconductors ZnS: Cu, Al dispersed as nanocrystalline green phosphors in xerogel with various lifetime components. The sol-gel silica-based phosphors are characterized by unusual valence states of the transition metal ions, stable centres in organic-inorganic hybrid hosts and the 500 ps lifetimes of D-A pairs due to spd hybridization effects in semiconductor nanocrystals.

Key words: *luminescence; sol-gel glass; nanocrystal; LMCT; phosphor*

## 1. Introduction

The sol-gel technique has developed very quickly in recent years, becoming an essential chemical method to prepare very small particles of nanometre sizes. Bhargava et al. [1] reported novel luminescence properties of nanocrystalline ZnS: $Mn^{2+}$ and demonstrated an ultra-short emission lifetime of the orange band obtained with a high quantum efficiency. Several papers have appeared since then on luminescence of nanocrystalline materials related to quantum confinement effects in semiconductors [1, 2]. Reisfeld and her group have reported optical properties of luminescent species, such as semiconductor quantum size particles and rare earth ions in sol-gel glasses

---

*Paper presented at the International Conference on Sol-Gel Materials, SGM 2003, Szklarska Poręba, Poland.

**Corresponding author, e-mail: morita@ch.seikei.ac.jp.

and zirconia films which are characterized by quantum confinement effects [3–6]. Moreover, organic dye-based lasers were developed by the sol-gel technology [7]. We have investigated luminescence properties of sol-gel xerogel and silica glasses doped with transition metal and rare earth ions in order to develop nanocrystalline phosphors in which the surface enhancement effect induces unusual band shifts to blue and shortening of lifetimes due to surface defects or spd mixing effects [8]. In this paper, we present sol-gel derived nanoparticles such as metal ions and nanocrystals dispersed in xerogel and sol-gel $SiO_2$ glasses for phosphors with interesting luminescence properties. The particles with a diameter of 5–10 nm emit in the blue-green-red spectral regions. In the following, we characterise the optical properties, lifetimes, Stokes shifts, and temperature dependences of various materials.

## 2. Experimental procedures

We have prepared phosphors according to the following sol-gel procedures. TEOS (tetraethooxysilane $Si(OC_2H_5)_4$), DEDMS (diethoxydimethylsilane), metal nitrate (1–0.5 mol %) were dissolved in a solution of water and ethyl alcohol and the solution was stored at room temperature. Xerogel was obtained after 2–3 months as wet solid blocks which, after annealing at 600 °C for one day, turned into transparent and isotropic sol-gel glasses containing dopants. By optimizing the preparation conditions, we can obtain glassy materials of desired optical qualities. Luminescence and luminescence excitation spectra, time-resolved spectra and lifetimes were measured in the temperature range between 10 and 300 K using a computer controlled luminescence spectrophotometric system combined with a Spex 1401 double monochromator and $N_2$ laser (337.1 nm) as an excitation source, developed in our laboratory [8]. The luminescence in the near infrared spectral region was measured using a computer-controlled SPEX 1702 single monochromator with a cryogenic system [9]. For rapid availability of luminescence and time resolved luminescence data, we also utilized an ICCD detection system. In addition, ultra-short luminescence lifetimes between 50 ns and 10 ps were detected by a single photon counting system and a streak camera using a pico-second YAG: $Nd^{3+}$ laser excited dye laser second harmonic (300 nm, 250 fs) as an excitation source.

## 3. Experimental results and discussions

Various sol-gel derived doped luminescent materials have been developed in our laboratory. The dopants were classified into three groups: (1) transition metal and rare earth ions, (2) metal complexes, and (3) semiconductors. In order to emphasize their versatile applications, we describe their luminescence properties and the electronic structures by fluorescence colours in red, green, blue, white and NIR (Near-Infrared).

These materials are considered to be usable as nanoparticles in fabrication of displays, lamps and storage phosphors while their optical properties, the quantum efficiencies and the saturation currents are not as yet examined under cathode-ray irradiation or under electric fields applied.

### 3.1. Phosphors due to metal ion dopants

Phosphors with red colours can be obtained from $Cr^{6+}$ ion centres. Luminescence due to surface-activated $SiO_2$: V, Cr centres was reported by Anpo et al. [10]. As a typical example, luminescence of chromium ions doped in sol-gel silica glass No. 1 ($SiO_2$: $Cr^{6+}$) at 10 K is shown in Fig. 1.

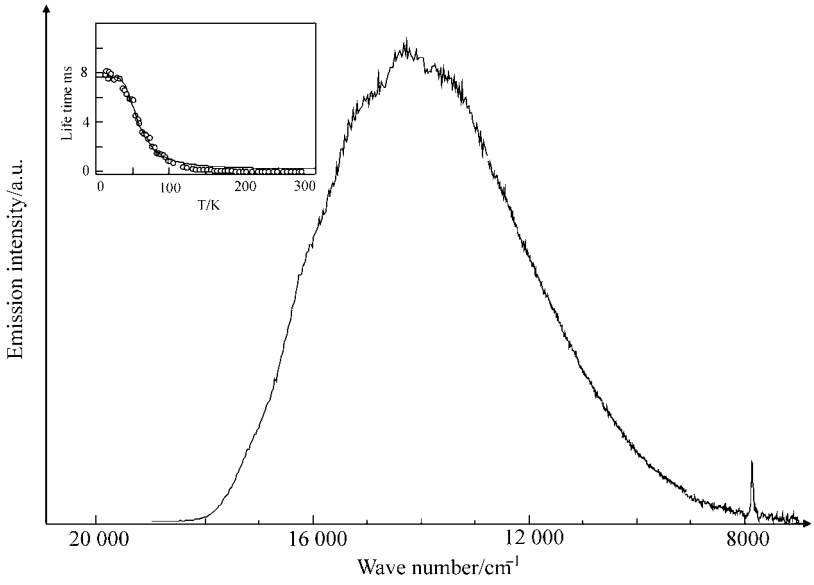


Fig. 1. Luminescence spectrum of the sol-gel glass $SiO_2$: Cr (sample No. 1) at 10 K, annealed at 800 K for 24 hrs, under $N_2$ laser excitation. The inset shows the temperature dependence of the average lifetime

The broad red band centred at 15 400 $cm^{-1}$ is due to highly oxidized chromium(VI) ions in tetrahedrally coordinated $[CrO_4]^{2-}$ complex centres. The bright emission has a lifetime of 8 ms and 0.02 ms at 10 K and 300 K, respectively. This emission was once ascribed to chromium(V) ions with a single d-electronic configuration in view of the band shape and its position [11]. Later, the temperature dependence of lifetimes and ESR data were found to be consistent with a model scheme of tetrahedrally oxo-coordinated $[MO_4]$ centres of chromium(VI) ions with the closed-shell electronic structure. Luminescence is associated with the $^3$LMCT (Ligand to Metal Charge Transfer) transition mechanism. The progressive structure of the broad band results

from vibronic interaction of the M–O stretching mode [12]. In the course of redox reaction, chromium(III) is oxidized to chromium(VI) ions. Therefore, the xerogel and glasses should contain residual chromium ions with the intermediate valence, i.e. chromium(IV) and chromium(V). Strek et al. reported the luminescence of a similar $SiO_2$: Cr glass, which was completely oxidized by annealing at 1300 K under oxygen gas flow [13].

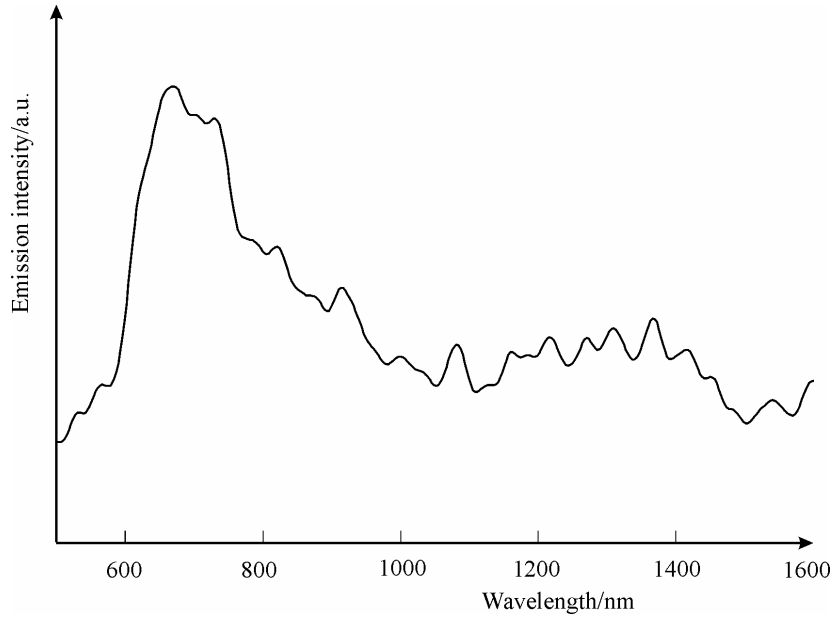


Fig. 2. Luminescence spectrum of $SiO_2$: Cr (sample No. 2) sol-gel glass at 10 K in the NIR spectral region. The sample was prepared at 1300 K under oxygen gas flow

Figure 2 shows the VIS-NIR luminescence at 10 K of the Cr-doped sol-gel silica glass sample (No. 2) ($SiO_2$: Cr) prepared by Strek and his group. The asymmetric band shape around 700 nm suggests the presence of complex centres in the glass. By taking into account the ESR data, the emission band in the deep-red (650–850 nm) region was ascribed to tetrahedrally coordinated Cr(VI) ions associated with Cr(V) ions. We have found vibronic structures and the associated side band at 1300 nm in the emission spectra. The side band is tentatively assigned to $Cr^{4+}$ ions, known in forsterite ($Mg_2SiO_4$: $Cr^{4+}$) as a band at 1.13–1.36 μm.

Further experiments are needed to obtain spectroscopic evidence of Cr(VI, V) centres. We have investigated the luminescence at 10 K of chromium(V) ions doped in sol-gel PLZT ceramics (Pb, Ln)(Zr,Ti)$O_3$ [14]. Figure 3 displays the luminescence of PLZT: Cr with a small peak and a broad emission band at about 740 and 1000 nm, respectively. The former is assigned to R lines of Cr(III) ions while the latter to Cr(V) ions of a nearly octahedral [$MO_{12}$] centre at the A site. If we assume the presence of tetrahedral $[Cr(V)O_4]^{3-}$ centres in $SiO_2$, the emission band should be found at a wave-

length longer than 1000 nm, by taking into account the crystal field splitting. We also prepared chromium-doped silica (90%)–alumina (10%) composites, $90SiO_2 \cdot 10Al_2O_3$: Cr. We found at 10 K a broad emission band at around 12 000 $cm^{-1}$ (830 nm). It is assigned to the U-band emission of chromium(III) ions in the $[AlO_6]$ site because the band position and long lifetimes are close to those reported in Cr-doped aluminosilicate glasses [15]. The alumina ($Al_2O_3$) doped in silica affords the Cr ion many chances to occupy the Al site and it does not promote efficiently the generation of Cr(VI) and Cr(V) ions while the valence of $Cr^{3+}$ remains unchanged in the condensation and redox reaction processes.

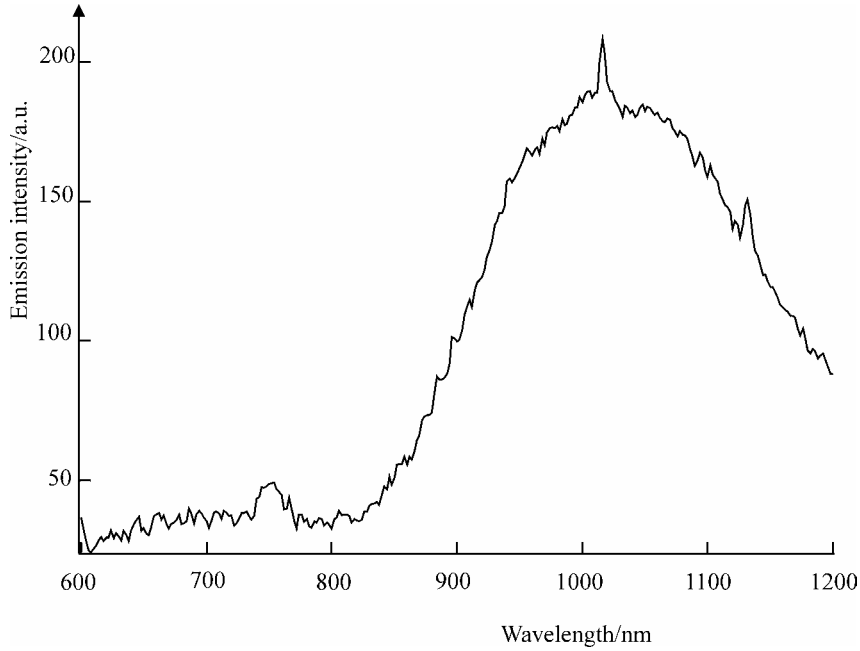


Fig. 3. Luminescence spectrum of PLZT(9/65/35); Cr (0.1%) at 10 K under Hg-arc (365 nm) excitation

Luminescence spectra of $KCrO_3Cl$ single crystals were measured at 10 K to elucidate luminescence characteristics of the $[Cr(VI)O_4]^{2-}$centre. The electronic structure of the centre is determined from the Stark experiments as a distorted tetrahedral $[Cr(VI)O_3Cl]$ centre of $C_{3v}$ point symmetry [16]. As shown in Fig. 4, the emission spectra are composed of a main band centred at 800 nm and a side band at 1400 nm. In comparison with emission of $SiO_2$: $Cr^{6+}$ (Fig. 2), two spectral profiles demonstrate a good correspondence while the band of $KCrO_3Cl$ shows a red shift of about 2000 $cm^{-1}$ by lifting the orbital degeneracy in $C_{3v}$ symmetry. By comparing these spectral features we conclude that the red band of Cr doped sol-gel silica glass is principally due to chromium(VI) ion being associated with $Cr^{3+}$, $Cr^{4+}$ and $Cr^{5+}$ centres.

We have described so far a red phosphor originating from $Cr^{6+}$ in $SiO_2$. Extending this research we doped into sol-gel glasses other transition metal ions with 3d, 4d, and

5d electronic configurations. With increase of principal quantum numbers of dopants with $n$ = 3, 4, 5, the spin-orbit interaction will be enhanced by the increase of atomic weight. Therefore the mixing of the wave function of the triplet and singlet states increases, resulting in the enhancement of lifetimes and of the fluorescence quantum efficiency. We have already reported luminescence spectral characteristics of 9 elements (Ti, V, Cr, Zr, Nb, Mo, Hf, Ta, W) doped in sol-gels at room temperature [12]. In this paper, we compare host-dependent phosphor properties. We found an increase of the luminescence intensity and enhancement of vibronic progressions in the luminescence of $V^{5+}$ in $SiO_2$ when a small amount of $Al_2O_3$ or $TiO_2$ was doped into $SiO_2$. As a result, quantum efficiency of this phosphor increased in the hybrid glass. In the case of a pure $SiO_2$ host, the dopant ion will occupy the substitutional centre in the tetrahedral structure of $SiO_2$. However, an addition of $Al_2O_3$ seems to efficiently strengthen the chemical bonding of the $SiO_2$ structure [10] because the transition metal ions will also be supported by the octahedrally coordinated centre. When the annealing temperature ($T_a$) of $SiO_2$: V was raised from 80 °C to 800 °C, luminescence quenching temperature ($T_q$) was found to be roughly proportional to the annealing temperature ($T_a$). In other words, we could use various parameters ($T_a$, $T_q$, activation energy, Stokes shift, electron-lattice interaction parameter $S$, etc.) as a measure of luminescence properties of sol-gel derived phosphors.

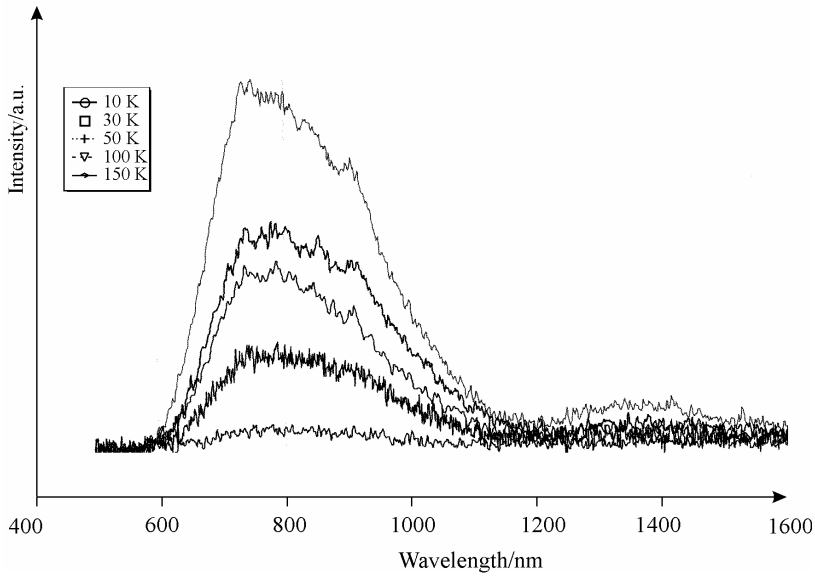


Fig. 4. Luminescence spectra of $KCrO_3Cl$ single crystal at 10 K under Hg-arc (365 nm) excitation as a function of temperature between 10 and 150 K

The phosphor in the NIR spectral region can be in principle realised by doping rare earth ions to make cooperative transitions possible. We have investigated the luminescence and lifetimes of sol-gel silica glasses co-doped with $Eu^{3+}$ and other lan-

thanide ions by luminescence and lifetime measurements. The rate of energy transfer from $Eu^{3+}$ to other ions is found to be strongly dependent on the trapping-limited relaxation processes in the solid [17]. Therefore, doping of more than two rare earth ions into the sol-gel silica glass is in principle not good enough to develop NIR phosphors. Instead, we have to improve chemical compositions of the host glasses [18].

### 3.2. Phosphors due to metal complex centres

Red phosphors are fabricated using $Eu^{3+}$ ions and complexes embedded in the sol-gel matrix. We first consider Eu(III) (15-CE-5)-doped sol-gel silica glasses where CE stands for a crown ether. This complex has a planar and pentagonal oxo-ligand with a $C_{5h}$ symmetry. The metal complex can be stabilized in the glasses if prepared under mild chemical conditions. The material is a composite of the organic ligand of (15-CE-5) and the inorganic Si and Eu(III) ions. In our experiments, we have not detected luminescence due to Eu(II) ions from xerogel [19]. By monitoring the splitting and the shift of Eu(III) ions in the $^5D_0 \rightarrow {}^7F_1$ transition, crystal field parameters have been determined in various samples as a function of annealing temperatures between 80 °C and 800 °C [8]. The metal complex was found to keep its axial symmetry when annealed at temperatures below 120 °C. Monitoring a variety of spectral changes, observed in the sol-gel glasses doped with the complex, we can establish the conditions of chemical preparation of new phosphors. If Eu is replaced by other rare earth ions and the ligand is chemically modified, improvements of colours, quantum efficiency, lifetimes and others become possible.

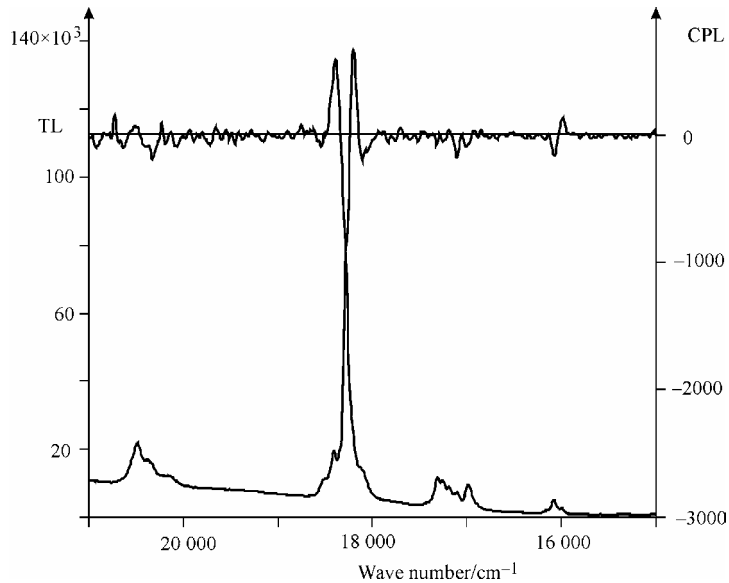


Fig. 5. Total luminescence (lower half) and circularly polarized luminescence (CPL; upper half) spectra of Tb(III)-(S)-cyclene derivative complex in xerogel at room temperature

To prepare a green phosphor, we started with Tb(III) ions or Tb complexes dissolved in sol-gel silica glasses. Luminescence spectrum of Tb(III) (15-CE-5) in the glass at 10 K shows a green band due to the host itself and associated peaks of $Tb^{3+}$. The quantum efficiency of this green band is not comparable to the commercial phosphor $Y_2O_3$: $Tb^{3+}$. However, the splitting of the sharp lines can clarify the electronic configuration of the green colour centre in the chiral host [8].

Figure 5 shows very special luminescence spectra of chiral phosphors: xerogel doped with optically active metal complexes of Tb-(S)-cyclene derivatives. The ordinate on the left side is the number of photons for total luminescence (TL) and the right ordinate is for the CPL signal. (CPL stands for circularly polarized luminescence which measures a differential signal between left- and right-handed circularly polarized luminescence.) If the optical active character of these complexes is maintained in the xerogel during the thermo-chemical treatments, we can see CPL spectral components clearly as those found for the complexes in solution. It is noteworthy that the existence of a chiral phosphor is demonstrated for the first time as a solid material.

Blue phosphors based on sol-gel glasses are not easy to prepare at present. This is because a blue to yellow band is inherent to the silica host itself. At lower temperatures, the host luminescence centred at 19 000 $cm^{-1}$ is enhanced in intensity and we cannot measure the luminescence component of the dopant ions. Nevertheless, emission of Ce(III)(15-CE-5) doped in xerogel consists of two bands, located at 24 000 and 19 000 $cm^{-1}$ with an interesting temperature-dependent spectral behaviour.

### 3.3. Phosphors due to semiconductor nanocrystals

Quantum confinement effects in luminescence of doped semiconductor nanocrystals are the most attractive topic of current research [20–22]. Our interest has been focused on nanocrystals embedded in ceramics and doubly doped nanocrystalline materials. Luminescence spectra of thin films of semiconductor CdS nanocrystals embedded in $ZrO_2$ ceramics were measured at 10 K [20]. The composite $80ZrO_2 \cdot 20CdS$ exhibits a broad band consisting of three emission bands originated from $ZrO_2$, CdS and defects. If $Eu^{3+}$ is doped in addition, a red phosphor appears due to the f-f transition located at 16 300 $cm^{-1}$. We observed a very fast luminescence decay of a few ns from the sample at room temperature [23]. The presence of a few ns lifetime components is interpreted as due to a non-radiative relaxation to defect centres near the surface.

Zinc sulfide doped with Cu-Al is a very important green phosphor for CRT applications. The origin of the luminescence is established as being due to the donor-acceptor pair transition. In Figure 6, the emission spectra of the green phosphors are displayed. Materials of different particle sizes, i.e. bulk powders and nanocrystal xerogels, were studied. The nanomaterial was prepared as ZnS: Cu-Al phosphor dispersed into sol-gel matrices. The preparation conditions are described elsewhere [24]. The two luminescence bands are similarly located at 20 000 $cm^{-1}$ with a bandwidth of 2500 $cm^{-1}$. Time-resolved luminescence spectra of this band show a red shift

with the increase of delay times from 1 to 15 μs at room temperature. The red shift of the green band and decrease of intensity with the increase of delay times are a good

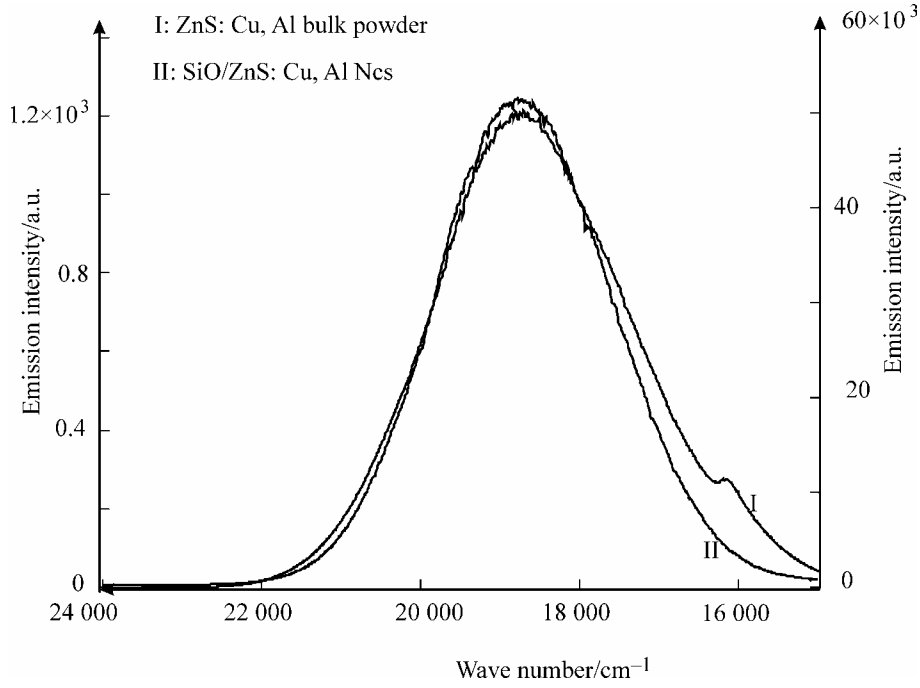


Fig. 6. Luminescence spectra ZnS: Cu, Al as bulk powder (I) and nanocrystals in xerogel (II) at room temperature under $N_2$ laser excitation

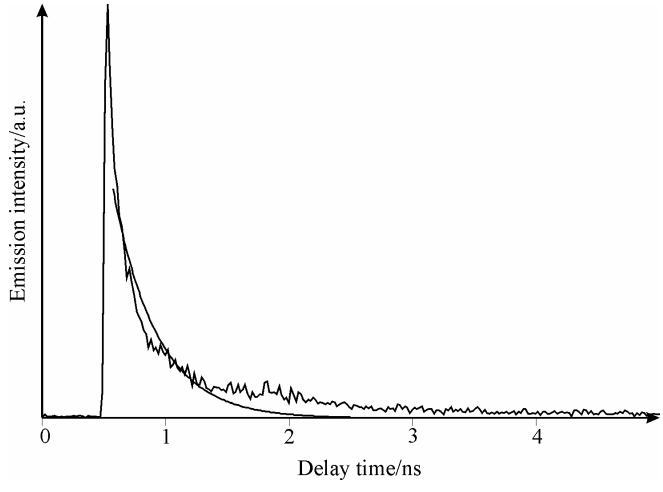


Fig. 7. Luminescence decay profile of ZnS: Cu, Al nanocrystals in xerogel at room temperature with a pico-second YAG: $Nd^{3+}$ laser exciting dye laser second harmonic (300 nm, 250 fs) as the excitation source. The lifetime is 355 ps assuming a single exponential decay curve

evidence of the donor-acceptor pair transition mechanism. However, the green phosphor in sol-gel glasses was found to reveal lifetimes of 500 ps at 10 K.

Figure 7 shows the luminescence decay profile of ZnS: Cu, Al nanocrystals in xerogel at room temperature. As an excitation source, the second harmonic of a dye laser excited with a pico-second YAG: $Nd^{3+}$ laser (300 nm, 250 fs) was employed. The lifetime is 355 ps by assuming a single exponential decay curve. The ultrafast relaxation processes were also found in $ZrO_2$/CdS: Eu and they are considered to be due to surface-bound defect centres. The fact that few μs and 0.5 ns lifetimes coexist in the same powdery material does support Bhargava's experimental findings. The green phosphor ZnS NCs is applicable to new storage phosphors of very fast optical response [25]. Preparation of this green phosphor is not so easy at the moment because the ZnS phosphor has Wurtzite structure at room temperature while the donor-acceptor mechanism is possible in the high temperature phase of the Zinc Blende structure. The material embedded in poly(vinyl alcohol) (PVA) matrices shows a blue luminescence due to SA (self-activated) centre. When the concentration of codopants (Cu, Al) is low, luminescence from the SA centre is dominant. Improvements of the preparation conditions are required.

## 4. Summary

We have presented chemical and optical properties of new phosphors based on xerogel and sol-gel silica glasses as host materials. In nanoporous and amorphous structures there exist traps, defects and killer centres which prevent efficient luminescence processes in amorphous solids. In the case of transition metal ions, broad and efficient luminescence bands in the visible spectral range (white and red) were found. They are due to LMCT transitions associated with dangling bonds on the surface. Quantum size-confinement effects were reported for nanocrystalline semiconductor materials. However, we could not find the same quantum effects in glasses because of the presence of trapping centres. Sol-gel $SiO_2$ glasses doped with rare earth(III) complexes are sensitive luminescence probes for monitoring structural changes of planar Eu(III) and chiral Tb(III) complexes. Luminescence properties of nanocrystalline phosphors were investigated in sol-gel $SiO_2$ glasses doped with ZnS: Cu, Al. These green phosphor nanocomposites have revealed a donor-acceptor transition within 0.02 ms decay times. The doped sol-gel xerogel and silica-based phosphors are characterized by the unusual valence states of the transition metal ions or stable rare earth complex centres in organic-inorganic hybrid hosts. Luminescence of green phosphors ZnS: Cu, Al in xerogel is characterized by the presence of 500 ps lifetimes due to spd mixing effects in semiconductor nanocrystals.

**Acknowledgements**

We are very grateful to W. Stręk for allowing us to use the sample No. 2 for measurements and to H. Kuroda for his continuous encouragement.

## References

[1] BHARGAVA R.N., GALLAGHER D., HONG X., NURMIKKO A., Phys. Rev.Lett., 72 (1994), 416.
[2] KUSHIDA T., TANAKA M., Bull. Stefan Univ., 14 (2002), 60 and references therein.
[3] REISFELD R., JOERGENSEN C.K., *Optical properties of colorants and luminescence species in sol-gel glasses*, [in:] *Structure and Bonding*, Vol. 77, R. Reisfeld and C.K. Joergensen (Eds.), Springer -Verlag, Berlin, 1992, pp. 207–256.
[4] REISFELD R., ZELNER M., SARAIDAROV T., MINTI H., *Semiconductor quantum size particles and rare earth ions ($Eu^{3+}$, $Tb^{3+}$), in amorphous sol-gel films*, [in:] *Advances on Energy Transfer Processes*, B. Di Bartolo, Xuesheng Chen (Eds.), World Scientific Publishing, 2001, p. 341.
[5] REISFELD R., GAFT M., SARAIDAROV T., PANCZER G., ZELNER M., Materials Letters, 45 (2000), 154.
[6] REISFELD R., J. Alloys Compds, 341 (2002), 56.
[7] REISFELD R., *Lasers based on sol-gel technology*, [in:] *Structure and Bonding*, Vol. 85, R. Reisfeld and C.K. Joergensen (Eds.), Springer-Verlag, Berlin, 1996, pp. 215–233.
[8] MORITA M., RAU D., KAI T., J. Lumin., 100 (2000), 97.
[9] HERREN M., MORITA M., J. Lumin., 66–67 (1996), 268.
[10] DZWIGAJ S., MATSUOKA M., ANPO M., CHE M., J. Phys. Chem., B104 (2000), 6012.
[11] HERREN M., NISHIUCHI N., MORITA M., J. Chem. Phys., 101 (1994), 4461.
[12] MORITA M., KAJIYAMA S., RAMI D., SAKURAI T., IWAMURA M., J. Lumin., 102–103 (2003), 608.
[13] STRĘK W., DEREŃ P.J., ŁUKOWIAK E., HANUZA I., DRULIS H., BEDNARKIEWICZ A., GAISHUN V., J. Noncryst. Solids, 288 (2001), 56.
[14] MURAKAMI S., HERREN M., RAU D., SAKURAI T., MORITA M., J. Lumin., 83–84 (1999), 215.
[15] GRINBERG M., HOLLIDAY K., J. Lumin., 92 (2001), 277.
[16] HØG J.H., BALLHAUSEN C.J., SOLOMON E.I., Mol. Phys., 32 (1976), 807.
[17] SHARMA P.K., JILAVI M.H., NASS R., SCHMIDT H., J. Lumin., 82 (1999), 187.
[18] BUDDHUDU S., MORITA M., MURAKAMI S., RAU D., J. Lumin., 83–84 (1999), 199.
[19] ZAITOUN M.A., GOKEN D.M., BAILEY L.S., KIM T., LIN C.T., J. Phys. Chem., B104 (2000).
[20] BOL A.A., MEIJERINK A., J. Phys. Chem., B105 (2001), 8861, 10197.
[21] BOL A.A., FERWERDA J., BERGWERFF J.A., MEIJERINK A., J. Lumin., 99 (2002), 325.
[22] KONISHI M., ISOBE T., SENNA M., J. Lumin., 93 (2001), 1.
[23] MORITA M., RAU D., FUJII H., MINAMI Y., MURAKAMI S., BABA M., YOSHITA M., AKIYAMA H., J. Lumin., 87–89 (2000), 478.
[24] MORITA M., BABA M., RAU D., KOIKE M., TAKADA K., ISHII T., YOSHITA M., AKIYAMA H., Nonlinear Optics, 29 (2002), 697.
[25] IHARA M., IGARASHI T., KUSUNOKI T., OHNO K., J. Electrochem. Soc., 149 (2002), 1172.

*Received 16 July 2003*
*Revised 6 October 2003*

*Materials Science-Poland, Vol. 22, No. 1, 2004*

# Analysis of ionisation energies of ions, ionic radii in a crystal lattice and the energy of electrons in ionic cores of metal atoms

ANDRZEJ STOKŁOSA*, JANUSZ ZAJĘCKI, STEFAN S. KUREK

Cracow University of Technology, Institute of Chemical Engineering and Physical Chemistry,
ul. Warszawska 24, 31-155 Kraków, Poland

An analysis of ionic radii, ionisation energies of ions and the electron binding energies in the highest occupied atomic orbitals of elements in their thermodynamically stable states is presented in the paper. It was shown that, for a number of ions of the same electronic configuration, several parameters, like the reciprocals of the ionic radii, square roots of ionisation energies and electron binding energies, are linear functions of the nuclear charge of ion (atomic number). A formal agreement of the character of the obtained relationships with the Slater equations describing the energies and the radii of electronic shells in atoms allows us to treat the constants in the obtained equations as an 'empirical' effective main quantum number and an 'empirical' screening constant.

Key words: *ion ionisation energy; electron binding energy; ionic radius*

## 1. Introduction

The development of modern chemistry, lasting for 150 years, in principle began with the discovery of periodic changes in properties of elements leading to the formulation of the periodicity law and the periodic table of elements. Advances in quantum chemistry allow us to determine quite precisely the electronic structures of atoms, the geometries of molecules and atomic interactions in molecules containing a significant number of atoms. One can even calculate interactions in solid state fragments comprising several tens of atoms by these methods. The density functional theory (DFT) proved to be the most successful in this area [1]. DFT calculations yield parameters of great importance to the materials chemistry. A simple concept of electronegativity can

*Corresponding author, e-mail: astoklos@chemia.pk.edu.pl.

be employed for the prediction of the stability of alloys, both electronegativity and hardness are applied in the calculation of the surface atoms properties, hence in explaining and predicting adsorption in such applications as catalysis and adhesion, just to name a few examples. DFT also enables one to obtain parameters of atoms on solid surfaces. It has also given, both chemical and physical, clear definitions of such paramount parameters as electronegativity and hardness of atoms and ions [2]. On the other hand, advances in experimental techniques and data obtained by these methods enable in many cases the theoretical models to be verified. They provide data on electron interaction energies not only in isolated atoms but also in atoms in crystalline structures. In spite of this great progress in gaining information concerning molecules and solid state structures, periodic changes in the properties of ions have remained a very important scientific problem. Approximate but simple correlations between relatively easily available values (such as the ionisation energy, the binding energies of electrons in given shells or the ionic radii and changes in properties of compounds formed by these ions) are very important in many areas of materials science, such as mineralogy, ceramics and metallurgy, in which the above parameters are sufficient to predict the geometries and properties of quite complex systems. It still remains open to what extent the complexity of the interactions of atoms in molecules or in crystal lattices changes their properties compared to the parent atoms or isolated ions or how it differentiates atom properties (in general depending on their surrounding).

One of the values characterising atoms and isolated (free) ions is their ionisation energy, a value that determines the energy with which an electron interacts with the atomic core containing a nucleus and the remaining electrons. The energy of the highest occupied Kohn–Sham orbital, used in DFT, will approach the negative of the first ionisation potential exactly [3]. Another similar value is the electron binding energy in the outermost filled electronic shell in atoms of elements in their thermodynamically stable forms. This energy characterises the atom core, the 'ion core' with valence electrons removed, in a state in which the atoms form metallic bonding in metals or atomic (homoatomic) bonding, for example, in the gas phase or in crystals of non-metals. The above parameters have an important feature of being absolute values, not derived from any models, and due to advances in spectroscopic methods are determined accurately.

Another parameter which defines the space occupied by an atom or an ion in a crystal is its radius, whose value can be estimated by various methods. Although it does not have any precisely defined physical sense, it allows us to formulate a useful working hypothesis, often employed in solutions of various problems in solid state chemistry. The concept of ionic radius is linked to an ion of a determined electric charge occurring in a crystal with dominating ionic interactions. It is therefore important to define the space occupied by the ion, i.e., the atom nucleus along with the electrons filling the electronic shells. The radius of the atom core is also used as a value of the ionic radius. Therefore, what is determined is the 'radius' of the outermost shell of, for example, $C^{4+}$ or $S^{6+}$ ions.

The ionisation potential of ions is employed in the discussion of variation of the properties of solids. Ionic radii, determined for ions in crystal lattices, are often used

in analyses of isolated ions. Swapping the values obtained for isolated ions with those obtained for ions in crystal lattices would be justified, provided that the differences between ions in such different environments were insignificant, which is generally not true.

In the present work, in spite of tremendous progress in quantum chemistry (particularly DFT), we would return to the problems mentioned above. Based on the values of ionic radii, which have been refined many times, and on accurately defined ion ionisation energies, we present their analysis. The aim of the analysis is to point out the differences between ions of the same electron configurations in various states and environments.

## 2. Ion ionisation enthalpy

Isolated ions have unperturbed structures. They can be quite precisely characterised due to the possibility of determining the energies of individual ionisation stages. For the analysis of the ionisation energies of ions of various charges, we have employed the enthalpy of their ionisation. The compiled results of several authors presented in handbooks and monographs [4–7] were the data source. Figure 1 presents a correlation between the nuclear charge of ion $Z$ and the square root of its ionisation energy, $E_{\mathrm{IE}}$, divided by the Rydberg constant $R$ (in the Rydberg's units). For example, for the $Al^{3+}$ ion, we took the fourth degree of ionisation of the aluminium atom.

The above correlation is presented for ions of the 2- and 10-electron configurations, for the 18- through 25-electron configurations, and for the remaining electron configurations in Figs. 1a–c. As can be seen in Figs. 1a and 1c, the above relationship is linear for a number of ions having the electron configurations of noble gases and the configuration of Ni (28 electrons), Pd (54), Pt (78) (with filled outermost (sp) shells and (d) subshells, respectively). This can be expressed by an equation of the general form

$$Z = a_{\mathrm{IE}}\sqrt{\frac{E_{\mathrm{IE}}}{R}} + S_{\mathrm{IE}} \tag{1}$$

Figure 1b, in turn, presents this relationship for the ionisation enthalpy of ions of unfilled valence (d) subshells. As can be seen, analogous linear relationships were obtained for ions of the same configuration and, what is more, of approximately the same slope as the line representing the 18-electron configuration. It should be noted that for a number of ions which do not occur as free ions, or in oxidation states that are even not postulated, the $\sqrt{E_{\mathrm{IE}}/R}$ values are located on extensions of the obtained lines or only slightly deviate from them. This includes, for example, $Fe^{5+}$, $Fe^{6+}$, $Fe^{7+}$ or higher oxidation states of Co and Ni ions.

In Figures 1a–c, the values of ionisation enthalpies of simple anions were shown for comparison, extracted from available data for electron affinities [4, 7, 8]. As can

Table 1. Parameters $a_n$ and $S_n^*$ of Eq. (1) for ions of the same electronic configuration of $N_c$ electrons

| Electronic configuration | Number of electrons of configuration $N_c$ | Parameters of Eq. (1) for ionisation enthalpy of ions | | | Parameters of Eq. (1) for electron binding energy | | | Effective principal quantum number, $n^*$ | Slater screening constant $S_s$ |
|---|---|---|---|---|---|---|---|---|---|
| | | Series of ions | $a_{IE}$ | $S_{IE}$ | Series of ions | $a_{EBE}$ | $S_{EBE}$ | | |
| $1s^2$ | 2 | $Li^+$–$F^{7+}$ | 0.996 | 0.652 | $Li^+$–$F^{7+}$ | 1.164 | 0.661 | 1.000 | 0.3 |
| 2(sp) | 10 | $Na^+$–$S^{6+}$ | 1.868 | 7.479 | $Na^+$–$Cl^{7+}$ | 2.550 | 7.132 | 2.000 | 4.15 |
| 2(sp) | 10 | $N^3$–$F^-$ | –3.311 | 10.655 | | | | | |
| $3s^2$ | 12 | $Si^{2+}$–$Cl^{5+}$ | 2.724 | 9.714 | | | | | |
| $3s^2p^2$ | 14 | $S^{2+}$–$Cl^{3+}$ | 2.609 | 11.827 | | | | | |
| 3(sp) | 18 | $K^+$–$Mn^{7+}$ | 2.662 | 14.861 | $K^+$–$Ca^{2+}$ | 4.839 | 13.386 | 3.000 | 11.25 |
| 3(sp) | 18 | | | | $Sc^{3+}$–$Mn^{7+}$ | 9.485 | 7.312 | | |
| 3(sp) | 18 | $S^2$–$Cl^-$ | –8.260 | 21.262 | | | | | |
| $3(sp)d^1$ | 19 | $V^{4+}$–$Cr^{5+}$ | 2.485 | 17.599 | | | | | |
| $3(sp)d^2$ | 20 | $Ti^{2+}$–$Mn^{5+}$ | 2.442 | 18.503 | | | | | |
| $3(sp)d^3$ | 21 | $V^{2+}$–$Mn^{4+}$ | 2.382 | 19.492 | | | | | |
| $3(sp)d^4$ | 22 | $Cr^{2+}$–$Fe^{4+}$ | 2.380 | 20.401 | | | | | |
| $3(sp)d^5$ | 23 | $Mn^{2+}$–$Co^{4+}$ | 2.368 | 21.265 | | | | | |
| $3(sp)d^6$ | 24 | $Fe^{2+}$–$Ni^{4+}$ | 2.315 | 22.518 | | | | | |
| $3(sp)d^7$ | 25 | $Co^{2+}$–$Ni^{4+}$ | 2.271 | 23.436 | | | | | |
| $3(sp)d^{10}$ | 28 | $Cu^+$–$Se^{6+}$ | 2.278 | 26.121 | $Zn^{2+}$–$Br^{7+}$ | 3.589 | 26.813 | | 21.85 |
| $4s^2$ | 30 | $Ge^{2+}$–$Br^{5+}$ | 3.105 | 27.057 | | | | | |
| $4s^2p^2$ | 32 | $Se^{2+}$–$Br^{3+}$ | 2.787 | 29.804 | | | | | |
| 4(sp) | 36 | $Rb^+$–$Mo^{6+}$ | 3.087 | 32.548 | $Rb^+$–$Sr^{2+}$ | 6.449 | 30.159 | 3.700 | 27.75 |
| 4(sp) | 36 | | | | $Y^{3+}$–$Mo^{6+}$ | 9.635 | 26.356 | | |
| 4(sp) | 36 | | | | $Tc^{7+}$–$Rh^{9+}$ | 13.353 | 20.147 | | |
| $5s^2$ | 38 | $Zr^{2+}$–$Mo^{4+}$ | 2.845 | 36.276 | | | | | |
| $4(sp)d^3$ | 39 | $Nb^{2+}$–$Mo^{3+}$ | 2.037 | 38.235 | | | | | |
| $4(sp)d^{10}$ | 46 | $Ag^+$–$Te^{6+}$ | 2.602 | 43.74 | $Cd^{2+}$–$Sn^{4+}$ | 4.557 | 43.946 | | 39.45 |
| $4(sp)d^{11}$ | 46 | | | | $Sb^{5+}$–$I^{7+}$ | 5.554 | 42.454 | | |
| $5s^2$ | 48 | $Sn^{2+}$–$Te^{4+}$ | 3.441 | 44.831 | | | | | |
| 5(sp) | 54 | $Cs^+$–$La^{3+}$ | 3.395 | 50.496 | $Cs^+$–$La^{3+}$ | 11.751 | 43.865 | 4.000 | 45.75 |
| $5(sp)d^1$ | 55 | $La^{2+}$–$Pr^{4+}$ | 2.299 | 54.254 | | | | | |
| $5(sp)d^{10}$ | 78 | $Au^+$–$Bi^{5+}$ | 3.025 | 75.244 | $Hg^{2+}$–$At^{7+}$ | 5.291 | 75.959 | | 71.85 |
| $6s^1$ | 79 | $Hg^+$–$Tl^{2+}$ | 3.262 | 76.168 | | | | | |
| $6s^2$ | 80 | $Tl^+$–$Bi^{3+}$ | 3.336 | 76.903 | | | | | |

*Subscript $n$ at constants denotes the values obtained by means of ionisation enthalpy (IE) and electron binding energy (EBE) at the outermost filled shell in atoms of elements in their natural form.

be seen, the $\sqrt{E_{IE}/R}$ values computed for anions show a deviation from the line determined for cations of the same electron configuration. Monovalent anions have values lower than those obtained from linear extrapolation, which indicates that electrons in isolated anions are bound relatively weaker than in cations of the same configuration. It should be emphasised that when a first electron is added to an atom the energetic effect is exothermic (anion ionisation potential has the same sign as in the case of cations), whereas adding the second electron is an endothermic process. Since the ionisation enthalpies of divalent anions are negative, the absolute values of $|E_{IE}|$ for anions were plotted in Fig. 1 merely for illustration.

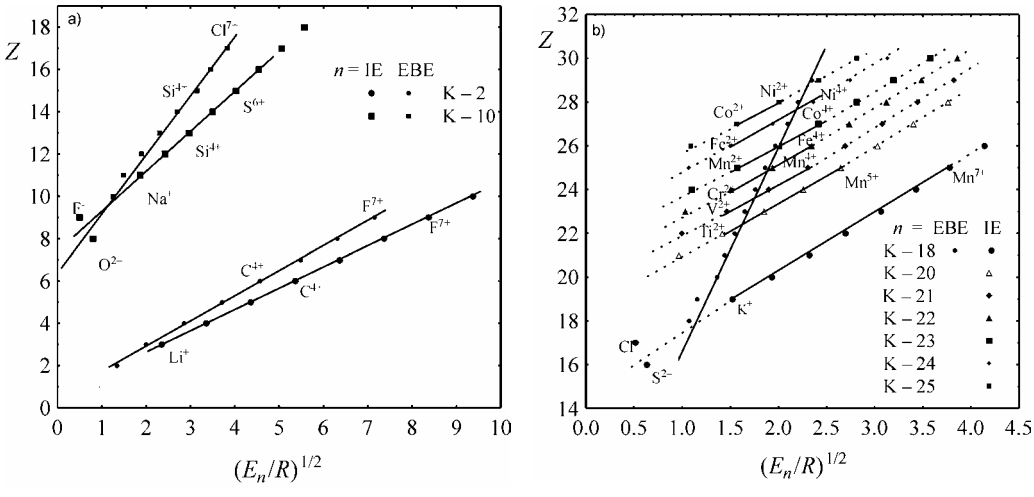


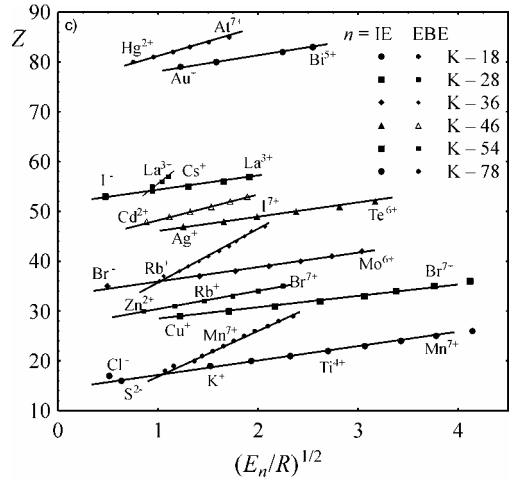


Fig. 1. Correlation between the nuclear charge of ion, $Z$, and the square root of ionisation enthalpy, $E_{IE}$ (in Rydberg's units) of $M^{z+}$ ions (ionisation degree ($z + 1$)) – filled points, and electron binding energy ($E_{EBE}$) in the shells corresponding to the outermost filled shell in atoms of elements (in their thermodynamically stable phases) – open points: a) for ions of He (K–2) and Ne (K–10) electron configurations, b) from K–18 to K–25 electron configuration, c) rare gas atom configuration: Ar (K–18), Kr – (K–36), Xe – (K –54) and the atoms of elements: Ni – (K–28), Pd – (K–46), Pt – (K–78)

In Figure 2, the dependence of the parameter $a_n$ on the number of electrons, $N_c$, in the given configurations is presented (the values of parameters $a_n$ for anions were not plotted in the figure). The symbols of elements shown next to the points denote series of ions of the same electron configuration taken for the calculation of the straight-line parameters. As can be seen from Fig. 2a, the value of the parameter $a_{IE}$ is close to unity for two-electron configuration, whereas it ranges principally between 2 and 3 for the remaining configurations. It can also be noticed that the points representing ions of noble gas configurations are set along a broken line (18, 36 and 54 electron configurations), whereas the points for ions of 28-, 46- and 78-electron configurations (Ni, Pd and Pt ion configurations) are set along a parallel line, significantly shifted. Other configurations stray away from the above lines.

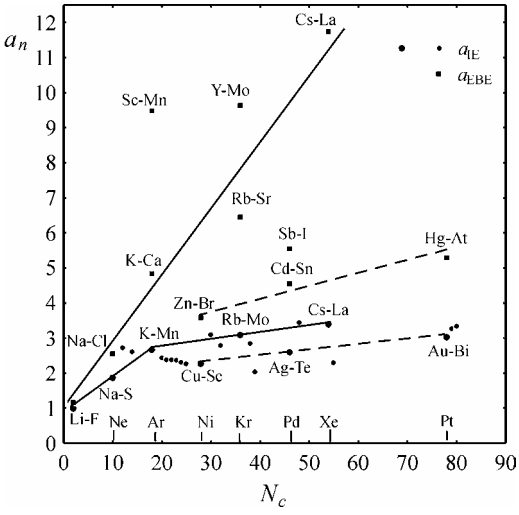


Fig. 2. Dependence of the coefficients $a_{IE}$ and $a_{EBE}$ of Eq. (1) on the number of electrons $N_c$ of respective electron configurations. The circles were based on ionisation enthalpies of ions, the squares were based on electron binding energy in the outermost filled shell (corresponding to the outermost shell of isolated ion) in atoms in their thermodynamically stable phases

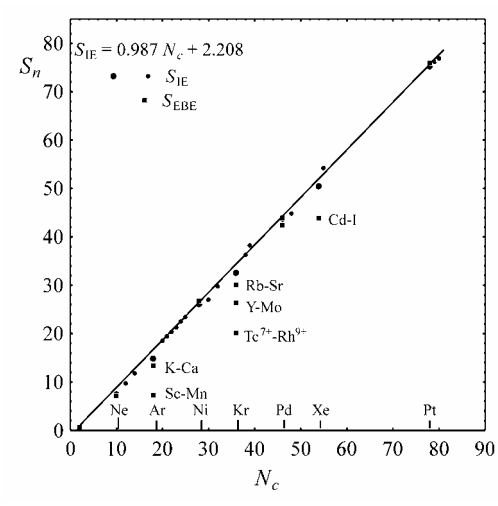


Fig. 3. Dependence of the coefficients $S_{IE}$ and $S_{EBE}$ (Eq. (1)) on the number of electrons $N_c$ of respective electron configurations. The circles were based on ionisation enthalpies of ions, the points were based on electron binding energies in the outermost filled shells (corresponding to the outermost shell of isolated ion) in atoms in their thermodynamically stable phases

Figure 3 presents the dependence of the parameter $S_{IE}$ on the number of electrons of respective electron configurations. As can be seen, the relation is practically linear and can be described by the equation:

$$S_{IE} = 0.987N_c + 2.208 \tag{2}$$

The parameters of the Eq. (2) were determined on the basis of the $S_{IE}$ values for ions of noble gas configurations as well as for ions of the configurations of Ni, Pd and Pt atoms. As can be seen, the values of $S_{IE}$ for other configurations do not lie far away from the above line.

## 3. Electron binding energy

Ionic cores (atoms stripped of valence electrons) in metals have analogous electron configurations as the ions discussed above. It is often believed that their properties are not very different from those of isolated ions. A value that characterises the ionic core in metals is the electron binding energy in the outermost filled shell of atoms of elements in their thermodynamically stable states (i.e., the states in which the cations stripped of their valence electrons are ‘bonded’ by metallic bonds). The above

energy should be close to ionisation energies of ions with filled (sp) shells or (d) subshells. For comparison, the binding energies of electrons in the shell which corresponds to the outermost shell of the above discussed isolated ions was plotted in Fig. 1 (data were taken from the literature [9–12]). The electron binding energies were determined for the elements in their natural form, hence neither for isolated ions, nor for ions in an ionic crystal. As can be seen in the figure, the dependences of the electron binding energies in a given shell, $\sqrt{E_{\mathrm{IE}}/R}$ , on $Z$, for various elements also exhibit a linear character in the discussed system of coordinates, but with a different slope. These divergences are quite obvious and result from the fact that the energy of electrons in the outermost filled shell is affected by interactions of covalent or metallic character occurring between atoms. It can therefore be seen that an electron in the 'ion core' in a metal is significantly weaker linked to the nucleus than an analogous electron in the outermost shell in an isolated ion, though it is generally assumed that electrons in (sp) shells do not take part in metallic bonding. A similar situation occurs in the case of molecules with atomic bonds. The linear character of the discussed relationship, presented in Figs. 1a–c, allows us to determine the parameters of linear equations such as Eq. (1). For some configurations though, the relationship was approximated by two or even three linear equations. In Figures 2 and 3, the dependences of those parameters on the number of electrons in the respective electron configurations are presented. As can be seen in the figures, the values of parameters $a_{\mathrm{EBE}}$ and $S_{\mathrm{EBE}}$, compared to the analogous parameters based on the ionisation enthalpy, demonstrate quite large differences. This shows that the state of an isolated ion is considerably different from the state of 'ionic' core of atoms of elements in their thermodynamically stable states. It specially refers to the parameters determined for a series of ions of higher charge, like $Sc^{3+}$–$Mn^{7+}$, $Y^{3+}$–$Mo^{6+}$, $Tc^{7+}$–$Rh^{9+}$, $Cd^{2+}$–$I^{7+}$.

It results from the presented analysis that differences between the binding energies of electrons in the outermost filled shells of atoms and ion ionisation potentials are so large that they cannot be interchanged in calculations.

## 4. Slater equations

The linear character of the dependence of ionisation enthalpy on the nuclear charge of ion obtained above is analogous to the Slater equation allowing one to calculate the energy of electronic shells in atoms [13–15]:

$$E_{\mathrm{S}} \frac{R(Z-S)^2}{\left(n^*\right)^2} \tag{3}$$

where: $E_{\mathrm{S}}$ is the energy of a Slater orbital, $R = m_{\mathrm{e}} e^4 / 8\pi^2 \varepsilon_0^2 \hbar = 13.5984$ eV is the Rydberg constant, $Z$ is nuclear charge, S is screening constant, $n^*$ stands for the effective main quantum number. The values of the main quantum number given by Slater for

the respective shells allow a better agreement between results of quantum-mechanical calculations and those obtained from experiments to be achieved. By rearranging the above equation, we get a relationship which is analogous to Eq. (1):

$$Z = n^* \sqrt{\frac{E_S}{R}} + S \tag{4}$$

It results from comparing Eqs. (1) and (4) that the proportionality coefficient $a_{IE}$ can be treated as a parameter corresponding to the effective principal quantum number and the parameter $S_{IE}$ as a screening constant. The agreement is quite good, particularly because the values $S_S$ calculated on the basis of the Slater rules yield correct shell energies for elements with the atomic number lower than 18.

Quite large differences between the parameters $a_n$ and $S_n$ based on the electron binding energy in an appropriate shell and the ionisation enthalpy of ions confirm that the state of an isolated ion significantly differs from the analogous state of the 'ionic' core of atoms of elements in their thermodynamically stable physical states.

Modern quantum-mechanical methods allow the electron energy in the individual shells to be determined more precisely than the Slater equation, nevertheless, the functional character of both remains the same.

## 5. Ionic radii

In materials science one generally deals with inorganic solids, with ionic or ionic -covalent bonds linking the components of their structures. The ionic radius is meaningless in quantum chemistry, nevertheless, it can be a useful working hypothesis to determine the space occupied by an ion in a crystal lattice. The division of the distance between ions depends on the applied method of calculation of ionic radii. The size of this space depends on temperature due to vibrations of ions. Hence, the real 'ionic radius' is smaller than the radius of the space in which the ion is situated. The difference can be estimated on the basis of thermal expansion coefficients or by using the so-called integral expansion [16]. Based on these data, one can estimate that the relative change in the radii of ions in the temperature range of 0–298 K is smaller than 1%, i.e., within the error limits of ionic radius estimation. As mentioned above, the ionic 'radius' is a characteristic value for a given ion and depends mainly on the 'radius' of the outermost shell. The size of this radius will also depend on interactions of ions (positive and negative) as well as on the repulsion of electronic shells. These effects will largely depend on the number of the nearest neighbours, the latter (coordination number) depending mainly on the relative sizes of the ions forming the crystal. Interactions between ions also result in their polarization, due to which the interaction energy increases and hence the ionic radii decrease. The problem of 'ionic radius' is thus very complex and its magnitude can vary depending on the type of the compound.

Despite the above reservations concerning the ionic radii, we decided in the present work to proceed with the analysis, assuming that the ionic radii given in reference books have been repeatedly discussed and can consequently be regarded as verified. For the analysis were used the so-called Pauling's [4, 7, 17] and Shannon's ionic radii [4, 7, 18, 19], at present regarded as being the most reliable. The dependences of the reciprocal radii of ions of coordination number $n$ = 6 on the nuclear charge of ion is depicted in Fig. 4 for a number of electron configurations.

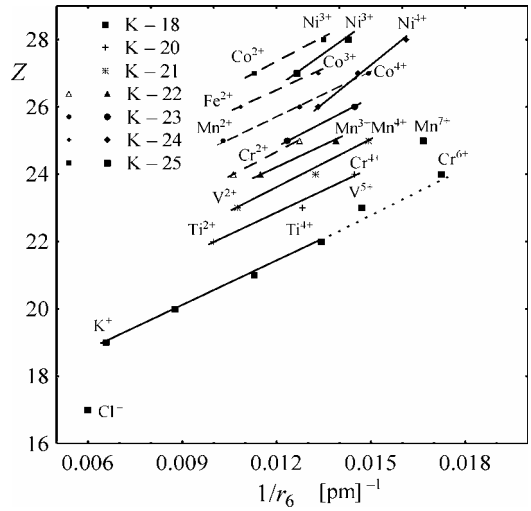


Fig. 4. Correlation between the nuclear charge of an ion and the reciprocal of radii of ions of coordination number $n$ = 6, for 18-(K–18), 20–25-(K–20 to K–25)-electron configurations. Open points denote the $1/r$ values for high-spin ions

As can be noticed, the dependences of the reciprocal of the ionic radius on the nuclear charge of ion are linear and have similar slopes not only for ions of argon atom configuration (with a filled (sp) shell) but also for ions of other configurations (incompletely filled (d) subshells). Only two configurations K–24 ($Fe^{2+}$–$Ni^{4+}$) and K–25 ($Co^{2+}$–$Ni^{3+}$) for ions of low spin states deviate from the pattern, whereas the lines for these ions in high spin states are parallel to the other lines. It is worth noting that while in the case of $V^{5+}$ and $Cr^{6+}$ ions only a small deviation occurs from the line determined for other ions of K–18 configuration, the $1/r_6$ value for manganese $Mn^{7+}$ ion shows a significant deviation from the determined line. Since the lines for electron configurations for ions containing more than 18 electrons are based on two or three values of ionic radii, considerable errors for the estimation of these parameters can be expected. Nonetheless, the slope, close to that of the line determined for cations of 18-electron configuration, justifies the correctness of the assumed relationships. Figure 5 presents the dependences of reciprocal ionic radii on the nuclear charge of ions for various coordination numbers. In Figure 5a, the above relationship is illustrated for configurations of the electron number $N_c$ = 2, 10, 12; in Fig. 5b, for 18–25 electron configurations, and in Fig. 5c, for 28, 34 and 46-electron configurations. As can be seen in the figures, the points of the discussed relationship lie on straight lines for ions of respective coordination numbers, nonetheless, their slopes exhibit quite large

differences. It is worth noting that the radius of $C^{4+}$ carbon ion of coordination number $n = 4$ is bigger than the radius of $B^{3+}$ ion and shows a considerable deviation from the line determined for ions of the tetrahedral configuration (Fig. 5a). Similarly, $Al^{3+}$ ion has the same radius as the magnesium ion and also demonstrates a significant deviation from the line determined for ions of the tetrahedral configuration. Its radius is close to that of the ion of the octahedral configuration. This demonstrates that these ions have relatively larger radii than cations of the same configuration. It can be generally concluded that cations of the charge higher than four systematically exhibit a deviation from the line determined for cations of a small charge. This deviation from the linear relationship can therefore be related to an increasing contribution of the covalent bonding to the interactions between atoms.

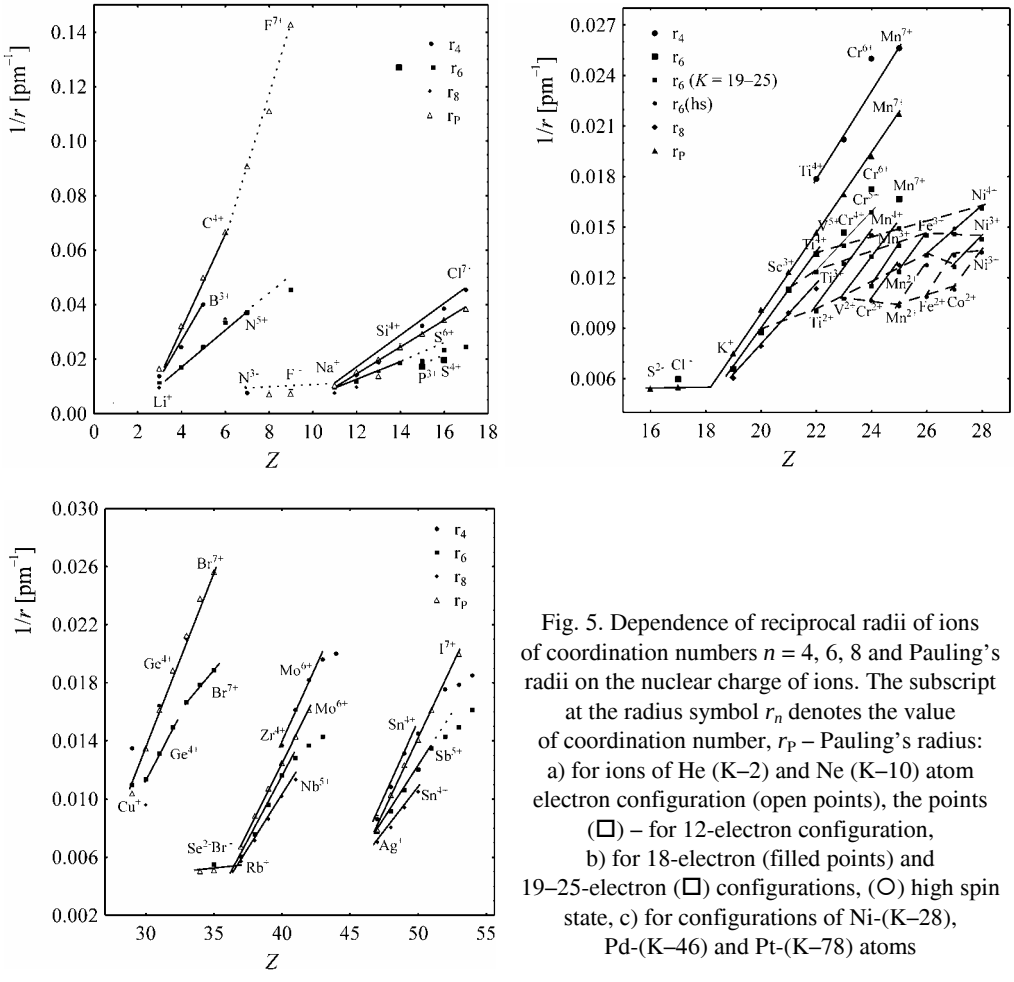


Fig. 5. Dependence of reciprocal radii of ions of coordination numbers $n = 4$, 6, 8 and Pauling's radii on the nuclear charge of ions. The subscript at the radius symbol $r_n$ denotes the value of coordination number, $r_P$ – Pauling's radius: a) for ions of He (K–2) and Ne (K–10) atom electron configuration (open points), the points (□) – for 12-electron configuration, b) for 18-electron (filled points) and 19–25-electron (□) configurations, (○) high spin state, c) for configurations of Ni-(K–28), Pd-(K–46) and Pt-(K–78) atoms

A substantial deviation of the $1/r_a$ value for anions from the line determined for cations of the same electron configuration (Fig. 5) is somewhat surprising. If the cor-

relations were correct, the radii of anions should be considerably bigger than estimated. Smaller radii of anions can be due to a contribution of covalent interactions between cations and anions, as well as between anions. It should be noted that the radii of dinegative ions and even the radius of the trinegative nitrogen ion are not considerably smaller than the radii of mononegative ions. This feature indicates that the participation of covalent interaction in the bonding with these anions is even larger. The situation is thus opposite to the case of isolated anions of halogens, in which a decrease in the interaction energy of the last electron was observed, which is equivalent to an increase in the radius of the isolated ion. It can therefore be assumed that the anions in crystals behave as ions of a higher hypothetical nuclear charge, thus a higher atomic number should be assigned to them.

The linear character of the relationship between the reciprocal of ionic radii and the atomic number for a number of ions of a given configuration allows the parameters of the straight line to be determined according to the equation:

$$Z = \frac{a_r}{\frac{r}{a_0}} + S_r \tag{5}$$

The radii of ions are expressed in terms of atomic units of length after dividing them by the radius of the first hydrogen atom orbit ($a_0 = 5.29\times10^{-9}$ cm). The straight-line parameters were determined for the points randomly arranged alongside a straight line. The correlation coefficient for the obtained linear function was $R = 0.99975$.

Figure 6a presents the dependence of the parameter $a_n$ on the number of electrons in the given electron configurations for ions of the coordination numbers $n = 4$ and 8, as well as for Pauling's ionic radii. They were also compared to the analogous parameters of the straight lines based on ionisation of the corresponding ions of the same configuration. The series of ions of the same electron configuration which were taken for computing the straight-line parameters are marked by the symbols of the elements next to the plotted points. As can be seen, the character of the relationship is similar to the analogous relationship based on ionisation enthalpies. A monotonous increase in the parameter $a_n$ with the number of electrons in the configuration is observed and, for the respective coordination numbers, this relation can be described with two or three linear functions. Due to a relatively high number of ions of coordination number $n = 6$ and of various electron configurations, an analogous comparison of the dependence of parameters $a_{IE}$ and $a_6$ on the number of electrons of the ion electron configuration is presented in Fig. 6b. As can be seen in the above figure, the values of the parameter $a_n$ are arranged in a relatively narrow range for a majority of electron configurations, practically along the broken line. A certain deviation occurs for configurations with over 22 electrons, particularly for the 24- and 25-electron configurations mentioned previously, as well as for 38–42- and 68-, 70- and 72-electron configurations. The points entering the correlation were determined based on two or three values of ionic radii, hence the above deviations can hardly be ascribed to erro-

Table 2. Parameters $a_n$ and $S_n^*$ of Eq. (5) for ions of the same electronic configuration of $N_c$ electrons

| Configu-ration | $N_c$ | Ions | $a_4$ | $S_4$ | Ions | $a_6$ | $S_6$ | Ions | $a_8$ | $S_8$ | Ions | $a_P$ | $S_P$ |
|---|---|---|---|---|---|---|---|---|---|---|---|---|---|
| 1 | 2 | 3 | 4 | 5 | 6 | 7 | 8 | 9 | 10 | 11 | 12 | 13 | 14 |
| $1s^2$ | 2 | $Li^+$–$B^{3+}$ | 1.420 | 2.043 | $Li^+$–$N^{5+}$ | 2.735 | 1.445 | | | | $Li^+$–$C^{4+}$ | 1.126 | 2.033 |
| $1s^2$ | 2 | | | | | | | | | | $N^{5+}$–$F^{7+}$ | 0.716 | 3.646 |
| 2(sp) | 10 | $Na^+$–$Cl^{7+}$· $(Al^{3+})^{**}$ | 3.063 | 9.763 | $Na^+$–$Si^{4+}$ | 5.734 | 8.436 | $Na^+$–$Mg^{2+}$ | 8.860 | 7.448 | $Na^+$–$Cl^{7+}$ | 4.024 | 8.748 |
| 2(sp) | 10 | $O^{2-}$–$F^-$ | 38.913 | –8.602 | | | | | | | $O^{2-}$–$F^-$ | 89.951 | –26.000 |
| $3s^2$ | 12 | | | | $P^{3+}$–$S^{4+}$ | 8.363 | 7.714 | | | | | | |
| 3(sp) | 18 | $Ti^{4+}$–$Mn^{7+}$· $(Cr^{6+})$ | 5.609 | 16.941 | $K^+$–$Ti^{4+}$ | 8.973 | 15.8 | $K^+$–$Ti^{4+}$ | 10.533 | 15.586 | $K^+$–$Mn^{7+}$ | 8.073 | 15.739 |
| 3(sp) | 18 | | | | | | | | | | $S^{2-}$–$Cl^-$ | 209.784 | –44.333 |
| $3(sp)d^1$ | 19 | $Cr^{5+}$–$Mn^{6+}$ | 4.022 | 19.611 | $Ti^{3+}$–$Cr^{5+}$ | 10.659 | 15.083 | $V^{4+}$–$Cr^{5+}$ | 7.692 | 18.267 | | | |
| $3(sp)d^2$ | 20 | $Cr^{4+}$–$Mn^{5+}$ | 6.106 | 18.125 | $Ti^{2+}$–$Cr^{4+}$ | 8.233 | 17.581 | | | | | | |
| $3(sp)d^3$ | 21 | | | | $V^{2+}$–$Mn^{4+}$ | 8.945 | 17.859 | | | | | | |
| $3(sp)d^4$ | 22 | | | | $Cr^{2+}$–$Mn^{3+}$ | 7.891 | 19.2 | | | | | | |
| $3(sp)d^4$ (hs) | 22 | | | | $Cr^{2+}$–$Mn^{3+}$ | 8.996 | 18.935 | | | | | | |
| $3(sp)d^5$ | 23 | | | | $Mn^{2+}$–$Fe^{3+}$ | 8.801 | 19.25 | | | | | | |
| $3(sp)d^5$ (hs) | 23 | | | | $Mn^{2+}$–$Co^{4+}$ | 8.180 | 20.521 | | | | | | |
| $3(sp)d^6$ | 24 | | | | $Fe^{2+}$–$Ni^{4+}$ | 13.478 | 16.525 | | | | | | |
| $3(sp)d^6$ (hs) | 24 | | | | $Fe^{2+}$–$Co^{3+}$ | 7.670 | 21.588 | | | | | | |
| $3(sp)d^7$ | 25 | | | | $Co^{2+}$–$Ni^{3+}$ | 11.611 | 19.222 | | | | | | |
| $3(sp)d^7$ (hs) | 25 | | | | $Co^{2+}$–$Ni^{3+}$ | 8.535 | 21.897 | | | | | | |
| $3(sp)d^{10}$ | 28 | $Zn^{2+}$–$Ge^{4+}$ | 7.045 | 24.939 | $Zn^{2+}$–$Ge^{4+}$ | 10.611 | 23.615 | | | | $Zn^{2+}$–$Br^{7+}$ | 7.659 | 24.446 |
| $3(sp)d^{10}$ | 28 | $As^{5+}$–$Br^{7+}$ | 8.127 | 23.893 | $As^{5+}$–$Br^{7+}$ | 14.280 | 20.594 | | | | | | |
| $4s^2$ | 30 | | | | $Ge^{2+}$–$Se^{4+}$ | 9.073 | 26.437 | | | | | | |
| 4(sp) | 36 | $Zr^{4+}$–$Mo^{6+}$ | 8.410 | 33.878 | $Rb^+$–$Nb^{5+}$ | 9.987 | 33.896 | $Rb^+$–$Nb^{5+}$ | 13.134 | 33.016 | $Rb^+$–$Mo^{6+}$ | 10.179 | 33.281 |

Table 2 cont.

| 1 | 2 | 3 | 4 | 5 | 6 | 7 | 8 | 9 | 10 | 11 | 12 | 13 | 14 |
|---|---|---|---|---|---|---|---|---|---|---|---|---|---|
| 4(sp) | 36 | | | | | | | | | | $Se^{2-}$–$Br^{-}$ | 243.207 | –31.000 |
| $5s^2$ | 38 | | | | $Nb^{3+}$–$Tc^{5+}$ | 19.986 | 28.674 | | | | | | |
| $4(sp)d^3$ | 39 | | | | $Mo^{3+}$–$Ru^{5+}$ | 16.985 | 31.324 | | | | | | |
| $4(sp)d^4$ | 40 | | | | $Ru^{4+}$–$Rh^{5+}$ | 14.157 | 34.143 | | | | | | |
| $4(sp)d^5$ | 41 | | | | $Ru^{3+}$–$Rh^{4+}$ | 14.334 | 34.750 | | | | | | |
| $4(sp)d^6$ | 42 | | | | $Ru^{3+}$–$Pd^{4+}$ | 22.971 | 29.900 | | | | | | |
| $4(sp)d^{10}$ | 46 | $Ag^{+}$–$Sn^{4+}$ | 9.608 | 42.489 | $Ag^{+}$–$Sb^{5+}$ | 13.125 | 41.62 | $Ag^{+}$–$Sn^{4+}$ | 15.938 | 41.106 | $Ag^{+}$–$I^{7+}$ | 9.593 | 42.845 |
| 5(sp) | 54 | | | | $Cs^{+}$–$La^{3+}$ | 12.565 | 51.402 | $Cs^{+}$–$Ce^{4+}$ | 15.271 | 50.756 | $Cs^{+}$–$Ce^{4+}$ | 14.239 | 50.487 |
| 5(sp) | 54 | | | | | | | | | | $Te^{2-}$–$I^{-}$ | 180.341 | 8.800 |
| $5s^2p^6$ | 68 | | | | $Yb^{2+}$–$Ta^{5+}$ | 13.036 | 64.051 | $Yb^{2+}$–$Ta^{5+}$ | 15.701 | 63.516 | | | |
| $5s^2p^7$ | 68 | $Hf^{4+}$–$Re^{7+}$· ($Ta^{5+}$) | 10.370 | 64.342 | $Hf^{4+}$–$Re^{7+}$ | 18.254 | 60.695 | | | | | | |
| $6s^2d^0$ | 70 | | | | $Ta^{3+}$–$Os^{6+}$ | 18.079 | 61.916 | | | | | | |
| $6s^2d^2$ | 72 | | | | $Os^{4+}$–$Ir^{5+}$ | 17.219 | 64.167 | | | | | | |
| $5(sp)d^{10}$ | 78 | $Hg^{2+}$–$Pb^{4+}$ | 10.452 | 74.919 | $Hg^{2+}Pb^{4+}$ | 13.164 | 74.243 | $Hg^{2+}$–$Tl^{3+}$ | 17.124 | 72.941 | $Au^{+}$–$Bi^{5+}$. ($Hg^{2+}$) | 12.219 | 74.260 |
| $5(sp)d^{10}$ | 78 | | | | $Bi^{5+}$–$At^{7+}$ | 18.018 | 72.241 | | | | | | |
| $6s^2$ | 80 | | | | $Tl^{+}$–$Po^{4+}$ | 17.574 | 75.194 | $Tl^{+}$–$Bi^{3+}$ | 19.766 | 74.885 | | | |
| 6(sp) | 86 | | | | $Fr^{+}$–$U^{6+}$ | 14.273 | 83.045 | $Ra^{2+}$–$Pa^{5+}$ | 16.922 | 82.473 | | | |
| $7s^2$ | 88 | | | | $Pa^{3+}$–$Pu^{6+}$ | 16.066 | 83.747 | | | | | | |

*Subscript *n* at constants denotes the values obtained by means of Pauling's radii (p) and Shannon's ionic radii for ions of coordination numbers *n* = 4, 6 and 8.

**( ) The ions, whose radii values have not been taken in calculation of the parameters of linear functions.

neous values of the ionic radii. The deviations can be related to ions of higher charge, mainly to 3d, 4d and 5d transition metal ions.

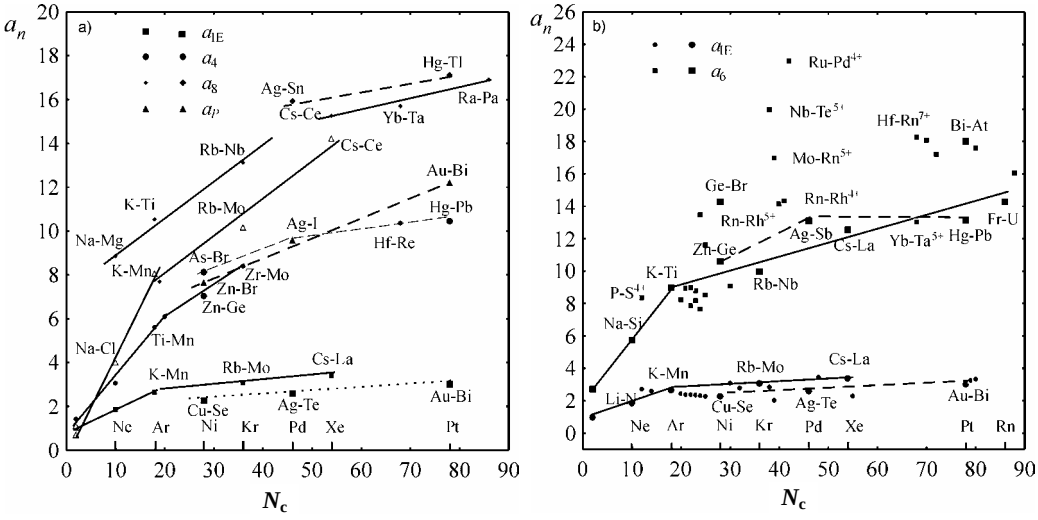


Fig. 6. Dependence of the parameter $a_n$ in Eqs. (1) and (5) on the number of electrons in ions of respective configurations: a) for ions of coordination number $n = 4$, 8 and Pauling's radii; the electron configurations of Ni, Pd and Pt atoms are denoted with filled points, b) for ions of coordination number $n = 6$. The electron configurations of filled shell ions (sp) (rare gas atoms) and subshell (d) (Ni, Pd and Pt atoms) are denoted with filled points

As the ionisation energies and the ionic radii characterise similar ions, the parameters in Eqs. (1) and (5) should be functionally related. Determining the ionic radii, Pauling assumed that the atom radius depends on the most probable distance of the outer (valence) electrons from the nucleus and that it is inversely proportional to the effective nuclear charge. Slater [13–15] postulated an analogous relationship for calculating atomic shell radii, showing that the maximum of the radial function occurs at the distance $r$ equal to:

$$r = \frac{\left(n^*\right)^2 a_0}{Z - S_S} \tag{6}$$

Rearranging Eq. (6), we obtain the equation:

$$Z = \frac{(n^*)^2}{\frac{r}{a_0}} + S_S \tag{7}$$

which is of an analogous type as the obtained experimental relationships (Eq. (5)). Thus, comparing the experimental relationships, (1) and (5), and the Slater equations, (4) and (7), we can see that if the ionisation enthalpy and ionic radii are expressed in

atomic units, then the following relation should exist between the coefficients in the above equations:

$$n^* \cong a_{\mathrm{IE}} = \sqrt{a_r} \tag{8}$$

Dependence of $a_{\mathrm{IE}}$ and $\sqrt{a_r}$ on the number of electrons of respective electron configurations of ions is presented in Fig. 7. Taking into account the fact that Eqs. (4) and (7) are approximate, the agreement seems to be very good, both in the character of the equation and in the values of $a_n$ themselves, in particular for ions of rare gas structure and ions of a small charge. As can be seen in Fig. 7, the dependence of $\sqrt{a_r}$ on the number of electrons in the configuration for given coordination numbers and a number of electron configurations of filled electron shells shows a much better linearity than that presented in Fig. 6. The remaining groups of ions, and in particular ions of a higher charge, deviate from the lines determined for the electron configurations mentioned above.

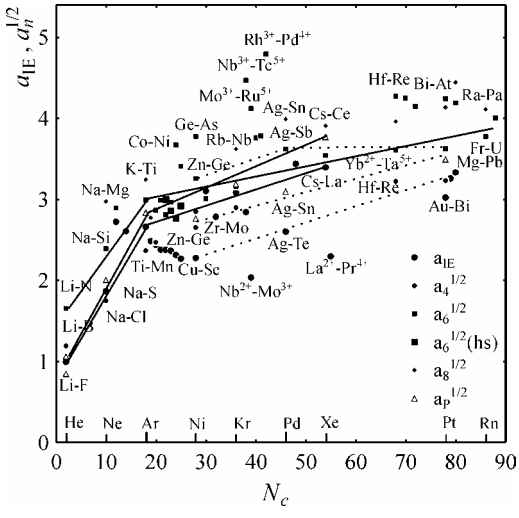


Fig. 7. Dependence of the parameters $a_{\mathrm{IE}}$ and $(a_n)^{1/2}$ in Eqs. (1) and (5) on the number of electrons in respective configurations. The points (■) denote the values of the parameter $a_6^{1/2}$ for ions of the coordination number $n = 6$ in their high spin states

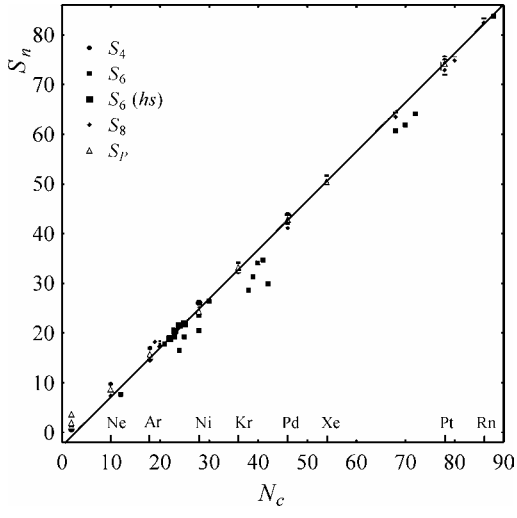


Fig. 8. Dependence of the $S_n$ parameters on the number of electrons of respective configurations for ions of coordination numbers $n = 4$, 6, 8 and Pauling's radii ($S_P$). The points (■) denote the ions in their high spin states. The straight line was plotted on the basis of the ionisation enthalpies of ions of filled electronic shells (Eq. (2))

Figure 8 presents the dependence of the parameter $S_n$ on the number of electrons for the discussed electron configurations. The solid line represents the relationship calculated for the points based on ion ionisation enthalpy (Eq. (2)); the points used in the calculations have not been shown for clarity. As can be seen, the values of the parameter $S_n$ agree quite well with the values of the parameters based on ion ionisa-

tion enthalpy, in particular for filled shell ions. Quite significant deviations, for instance in the case of the parameter $a_n$, occur for ions of 3d and 4d metals of a higher charge and of previously discussed configurations. A relatively good agreement is also observed between the parameter $S_n$ and the values of the screening constant calculated according to the Slater rules.

## 6. Conclusions

The following conclusions can be drawn from the above analysis of the ion ionisation enthalpy and their radii:

A number of cations of the same electron configuration and of the charge of 1–4 and beyond demonstrate a linear relationship between the reciprocal of the ion radius or the square root of their ionisation enthalpy and the nuclear charge of the ion (atomic number).

The agreement between the relations determined experimentally and the Slater equations describing the radius of an electronic shell and the electron energy in that shell demonstrates that the coefficients $a_{\mathrm{IE}}$ and $(a_n)^{1/2}$ as well as $S_n$ in Eqs. (1) and (5) can be referred to as the 'experimental' effective principal quantum number and the 'experimental' screening constant, respectively, and the difference $(Z - S_n)$ can be called the 'experimental' effective nuclear charge of the ion. These values can be applied to characterise the ions.

As expected, it results from the analysis of the parameters of experimental equations of the type (1) and (5) that the states of isolated ions and ions in crystals described on the basis of ionisation energies, electron binding energies and ionic radii are different. In particular, significant differences occur in the case of ions having electrons in the (d) subshell. The state of the analogous 'ion' core in atoms of metals is also considerably different.

### References

[1] SLATER J.C., *The Self-Consistent Field Method for Molecules and Solids*, McGraw-Hill, New York, 1974, Vol. 4.
[2] PEARSON R.G., *Chemical Hardness*, John Wiley, New York, 1997.
[3] LEVY M., PERDEW J.P., Phys. Rev. A, 32 (1985), 2010.
[4] HUHEEY J.E., KEITER E.A., KEITER R.L., *Inorganic Chemistry: Principles of Structure and Reactivity*, 4th Edition, Harper Collins, New York, 1993.
[5] *Handbook of Chemistry and Physics,* 79th Edition, D.R. Lide (Ed.), CRC Press, Boca Raton, Fl., USA, 1998.
[6] *Lange's Handbook of Chemistry*, 14th Edition, J.A. Dean (Ed.), McGraw-Hill, New York, 1992.
[7] WINTER M., WebElements: University of Sheffield, England (www.webelements.com).
[8] JAMES A.M., LORD M.P., *Macmillan's Chemical and Physical Data*, Macmillan, London, 1992.
[9] BEARDEN J.A., BARR A.F., *Rev. Mod. Phys.*, 39 (1967), 125.
[10] CARDONA M., LEY L. (Eds.), *Photoemission in Solids. I. General Principles*, Springer-Verlag, Berlin, 1978.

[11] FUGGLE J.C., MORTENSSON N., J. Electron Spectrosc. Relat. Phenom., 21 (1980), 275.
[12] WILLIAMS G. http:/pubweb.bnl.gor/people/gwyn/ebindene.html (www.webelements.com).
[13] SLATER J.C., Phys. Rev., 36 (1930), 57.
[14] SLATER J.C., *Quantum Theory of Atomic Structure*, McGraw-Hill, New York, 1960.
[15] MCWEENY R., *Coulson's Valence*, Oxford Univ. Press., Oxford, 1979.
[16] CHOJNACKI J., Bull. Acad. Polon. Sci., Ser. A 123 (1951), 321.
[17] PAULING L., J. Am. Chem. Soc., 49 (1927), 765.
[18] SHANNON R.D., Acta Cryst., A 32 (1976), 751.
[19] SHANNON R.D., PREWITT C.T., Acta Cryst., B 25 (1969), 925; B 26 (1970), 1046.

*Received 13 June 2003*
*Revised 3 November 2003*

*Materials Science-Poland, Vol. 22, No. 1, 2004*

# Effective nuclear charge of an ion

ANDRZEJ STOKŁOSA*, JANUSZ ZAJĘCKI, STEFAN S. KUREK

Cracow University of Technology, Institute of Chemical Engineering and Physical Chemistry,
ul. Warszawska 24, 31-155 Kraków, Poland

An analysis of the effective nuclear charge of ions based on linear relationships of the reciprocal of an ionic radius or the square root of ionisation energy and the nuclear charge of the ion has been carried out. It has been demonstrated that the effective nuclear charge of an ion is significantly different from its formal charge. The obtained character of the relationship indicates that the postulated parameter can be employed to determine differences in properties of ions. It has also been shown that the differences occurring in the calculated effective nuclear charges of the ion permit one to differentiate its states. Namely, values based on ionisation enthalpy characterise ions of a given coordination number in a crystal lattice.

Key words: *effective nuclear charge*; *formal charge; ions*

## 1. Introduction

A parameter which characterises any atom or ion is the so-called effective nuclear charge, lower than the actual nuclear charge. It results from the screening of the nuclear charge of the atom by electrons of an atom other than the considered one. The effect of the screening of the nuclear charge by electrons was for the first time taken into account in the Moseley law [1]. The effective charge has been widely applied in quantum mechanical atomic orbital calculations, which were first vperformed by Slater [2]. The rules put forward by Slater [2], Clementi and Raymondi [3], Burns [4] and others defined the above parameter with increasing precision, allowing an increasing precision of quantum mechanical calculations. Pauling [5] employed the effective nuclear charge for the calculation of ionic radii as early as in 1927, and Allred and Rochow [6] used it for determining the electronegativity of elements. In the eighties, rapid advances in the computational modelling of crystals created a possibility for determining parameters characterising single atoms or ions in a structure, as well as interaction energy and the like [7–9]. Despite the ever-growing computational abilities

*Corresponding author, e-mail: astoklos@chemia.pk.edu.pl.

that we have now, our knowledge about the structure of solids is still unsatisfactory and does not allow quantum mechanics to be applied in a straightforward manner for the determination of properties of ions. The best results have been obtained with the density functional theory (DFT) which has become the theoretical method of choice in dealing with solid-state problems. However, even DFT requires a considerable amount of computing time, though much less than the Hartree–Fock methods. Thus there is a constant search for relatively simple parameters which would allow the properties of ions to be differentiated, and hence the properties of compounds to be determined.

Linear relationships between the reciprocal of the ionic radius or the square root of ionisation energy of ions and the atomic number, obtained in the previous work [10] for a relatively large number of ions of the same electronic configuration, exhibit a character analogous to the Slater equation [2]. They indicate that the difference between the nuclear charge of the ion and the parameter $S$ in the equation can be treated as an experimental effective nuclear charge of the ion.

Because of a continuous transition from covalent bonding to an ionic one, a question has been posed in the present work, whether the proposed effective nuclear charge based on such values as ionic radii or their ionisation energies, determined according to the method proposed in [10], can really be related to a formal charge of an ion and whether it can constitute a basis for determining a scale which would differentiate ions with regard to their electrostatic properties (in crystals with dominating ionic bonding).

## 2. Effective nuclear charge of an isolated ion and the ion in a crystal lattice

The analysis [10] of the dependences of a parameter related to the ionisation energy of an ion, $\sqrt{E_{\mathrm{IE}}/R}$, ($R$ being the Rydberg constant) and of the reciprocal of the ionic radius ($1/r$) on the nuclear charge of the ion, $Z$, demonstrated that for ions of the same electronic configuration the above relationship can be described by means of the following linear equations:

$$Z = a_{\mathrm{IE}}\sqrt{\frac{E_{\mathrm{IE}}}{R}} + S_{\mathrm{IE}} \tag{1}$$

$$Z = \frac{a_r}{\frac{r}{a_0}} + S_r \tag{2}$$

where: $a_{\mathrm{IE}}$ and $a_r$ are constants, $R$ is the Rydberg constant, $r$ – ionic radius, $a_0$ is the Bohr radius ($a_0 = 5.29 \cdot 10^{-9}$ cm). It was also shown that the parameter $S$ in the above

equations can be treated as a screening constant and the difference between the nuclear charge and the screening constant $(Z - S) = Z_{\text{eff}}$, as the effective nuclear charge. Thus there exists a formal similarity between the Slater equation [2] and the 'experimental' relationships described by Eqs. (1) and (2) [10]. Despite the entire complexity of electron structures of atoms, a simple model can be used to describe a number of ions of a small charge. In the model, the outermost electron at a distance $r$ equal to the 'ionic radius' is taken into account. An isolated ion interacts with the atom core (nucleus and the remaining electrons) with an energy equal to the ionisation energy and an ion in a crystal lattice or in a coordination compound with the energy of bonding of the outermost electron. It should be emphasized that the radii of ions forming the crystal lattice are treated formally in the above model. The radius defines a space occupied by the ion, the size of which results from the atom structure as well as from interactions of ions in the crystallographic structure of a given compound, resulting in optimum distances between the centres of mass of ions. The effective nuclear charge is therefore a parameter dependent on the space occupied by a given ion or accessible to it. As a result, the effective nuclear charge depends on the size of space attributed to a given ion. Furthermore, the concept of the effective nuclear charge assumes that the atom, despite the number of electrons being equivalent to its nuclear charge, is not 'electroneutral'. This is entirely consistent with the fact that atoms of elements, except for noble gas atoms, are in their unstable states and interact with each other forming determined bonds, i.e., they combine yielding molecules which occur in a gaseous or liquid state or form crystals.

A question thus arises, how does the magnitude of the effective nuclear charge of ions vary as a function of the nuclear charge of an isolated ion and of an ion placed in a structure of a given coordination number.

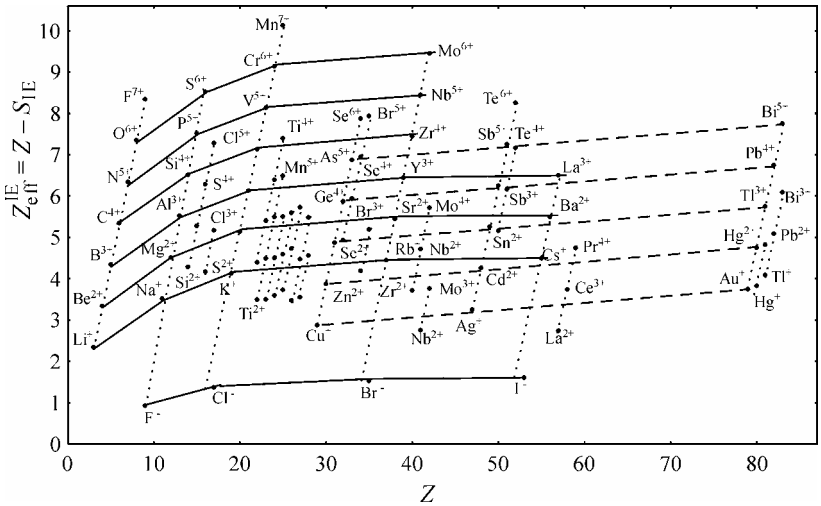


Fig. 1. Dependence of the effective nuclear charge of ions ( $Z_{\text{eff}}^{\text{IE}}$ ), based on values of ionisation enthalpies of ions, on the nuclear charge of ion (atomic number) $Z$

Figure 1 presents a dependence of the effective nuclear charge of isolated ions, $Z_{eff} = (Z - S_{IE})$, on the nuclear charge, $Z$, calculated according to Eq. (1) based on the ionisation enthalpy of ions [11–14]. As can be seen, the dependences of the effective nuclear charge of ions of the same electron configuration on the nuclear charge are fitted very well by straight lines. It should be noted that if the ion radius is assumed to be inversely proportional to its effective charge, then the radii of valence shells of isolated ions of noble gas structure (filled (sp) shells) having the same formal charge are smaller than the radii of ions of filled (d) subshells (electron configurations of Ni, Pd and Pt atoms).

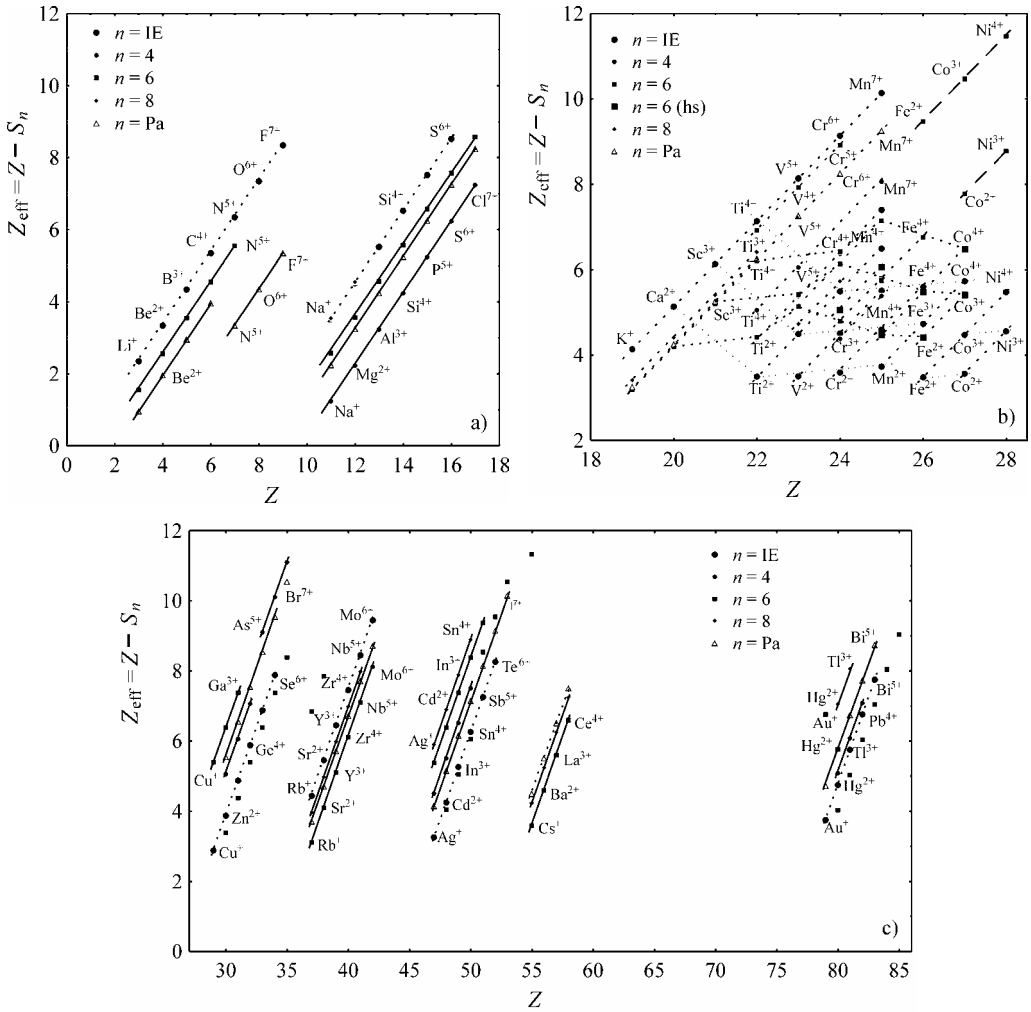


Fig. 2. Comparison of the effective nuclear charge of ion based on ionisation enthalpies of ions (subscript IE) and ionic radii for ions of the coordination number $n = 4$, 6 and 8, and Pauling's ionic radii (subscript Pa): a) for ions of electronic configuration of He and Ne atoms, b) for ions of 18-electron configuration (Ar) and 19–25-electron configurations (points (■) denote ions in high spin state), c) for ions of Ni, Kr, Pd, Xe, Pt atom configurations

Figure 2 shows a comparison of the effective nuclear charges of ions, calculated according to Eq. (2) based on ionisation enthalpies of ions and ionic radii [5, 14–16]. For comparison, Figs. 2a–c depict the effective nuclear charges of ions for ions of 2- and 10-electron configurations, for ions of 18–25-electron configurations and for ions of 28-, 36-, 46-, 54- and 78-electron configurations, respectively. As can be seen from the figures, the effective nuclear charges of isolated ions (of the same formal charge) are higher than the values based on ionic radii for a majority of ions of noble gas configurations. This indicates that the radii of isolated ions are smaller than the radii of the analogous ions in a crystal lattice. A reverse situation occurs in the case of ions of the electronic configuration of Ni, Pd and Pt atoms: for these configurations, the effective nuclear charges of isolated ions are smaller than for the analogous ions in crystal lattice. This in turn indicates that the ions in crystal lattice have smaller radii than the analogous isolated ions. These differences result from interactions between ions in crystal lattice: for the most part, the attraction between anions and cations and the repulsion between electron shells and ions of like charges. As a result, optimum distances between the centres of mass are established.

The effects mentioned can give rise to an increase in the radius of a sphere in which the ion is located, thus augmenting the 'ionic radius' in crystal lattice with respect to the radius of an isolated ion. The estimated radius of the space occupied by an ion in crystal lattice (at room temperature) includes also the effect of atom vibrations; it should therefore be bigger than the radius of the outermost electron shell of an ion. This is the case for ions of noble gas configurations, in which the valence shells are formed by (sp) orbitals. In the case of ions with the outermost shell formed by a filled (d) subshell, their polarisation interaction is significantly stronger than for ions of (sp) subshells, resulting in shortening of the distances between atoms. In such cases, both radii can be decreased. Otherwise, if a fixed anion radius is taken (which is assumed in a number of methods for radii determination), a decrease in the cation radius is found. A similar situation occurs in the case of radii of anions discussed in the previous work [10] which should be considerably larger, if they behaved as the cations of the same configuration. The aforementioned facts confirm the existence of a complex interactions of the ionic-covalent type.

The effective nuclear charge depends quite substantially on the coordination number, the highest values being attained by ions of coordination number 6 and considerably lower effective nuclear charge being exhibited by ions of coordination number 4. This is in agreement with the findings of Pearson [17] and Philips [18] that compounds of coordination number 6 are highly ionic, whereas those of the coordination number 4 are more covalent. It is worth noting that the values of the effective nuclear charge of ion based on Pauling's radii are most often close to the effective charge for ions of one of the coordination numbers.

The effective nuclear charges presented in Fig. 2b for ions of 18-electron (argon atom) configuration to 25-electron configurations allow the effective nuclear charges for ions of filled (sp) shells to be compared with ions of unfilled (d) subshells. As can be noticed, the points for the effective nuclear charges of ions of the same configura-

tion (more than 18 electrons), lie on straight lines, practically parallel to the lines set for the 18-electron configuration. This applies to the lines calculated both by using the ionic radii and ionisation enthalpies. It should be emphasised that the values of $Z_{eff}$ based on ionic radii are lower than the values of $Z_{eff}$ based on ionisation enthalpy as in the case of ions of 18-electron configuration. Thus the values of $Z_{eff}$ based on ionic radii are higher than those based on ionisation enthalpy for the configuration of more than 18 electrons (for ions of the same formal charge). These facts indicate that, similarly to the case of ions of filled (d) subshells, the ions of unfilled (d) subshells produce the effect of polarisation and their radii are smaller than those of isolated ions. It is worth noting that the effective nuclear charges of $Mn^{2+}$, $Fe^{2+}$, $Fe^{3+}$, $Co^{2+}$, $Co^{3+}$ and $Co^{4+}$ ions in their high spin states are quite well fitted by curves for ions of the same (formal) charge, whereas the values of $Z_{eff}$ for the above ions in their low spin states are significantly higher (open circles in Fig. 2b) – even higher than the values for the $Cr^{6+}$, $Mn^{7+}$ ions. These values can hardly be accepted as correct.

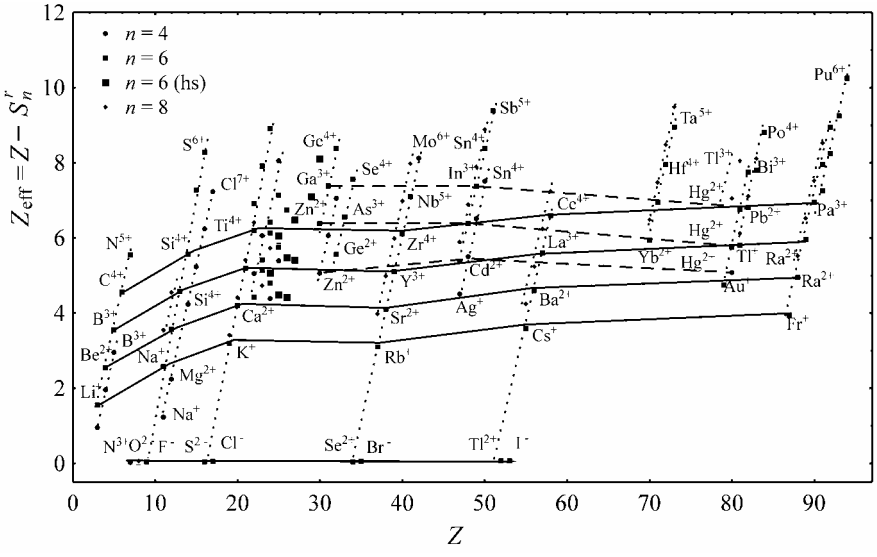


Fig. 3. Dependence of the effective nuclear charge of ions $Z_{eff}^{n}$ of coordination number $n = 4, 6, 8$ on the nuclear charge of ion $Z$ (points (■) denote ions in their high spin states)

Figure 3 summarises the effective nuclear charges based on their ionic radii, for ions of respective electron configurations and various coordination numbers. As can be seen, the character of the curves for ions of the same formal charge is similar as in the case of an analogous relationship of the effective nuclear charges of isolated ions calculated from the ionisation enthalpies (Fig. 1).

In Figures 1 and 3, the values of the effective nuclear charges of anions are also included. Since the values of $\sqrt{E_{IE}/R}$ or $1/r$ for anions deviate from the straight lines

Table. Values of effective charges of isolated ions $Z_{\mathrm{eff}}^{\mathrm{IE}}$ calculated on the basis of ionisation enthalpy (Eq. (1)) as well as ions of coordination number $n$ = 4, 6, 8 (superscript) calculated on the basis of Shannon's and Pauling's radii (superscript Pa); (hs) denotes ions in their high spin states

| Nuclear charge $Z$ | Ion | Formal charge $Q$ | Effective nuclear charge of ion | | | | | Nuclear charge $Z$ | Ion | Formal charge $Q$ | Effective nuclear charge of ion | | | | |
|---|---|---|---|---|---|---|---|---|---|---|---|---|---|---|---|
| | | | $Z_{\mathrm{eff}}^{\mathrm{IE}}$ | $Z_{\mathrm{eff}}^{\mathrm{Pa}}$ | $Z_{\mathrm{eff}}^{(4)}$ | $Z_{\mathrm{eff}}^{(6)}$ | $Z_{\mathrm{eff}}^{(8)}$ | | | | $Z_{\mathrm{eff}}^{\mathrm{IE}}$ | $Z_{\mathrm{eff}}^{\mathrm{Pa}}$ | $Z_{\mathrm{eff}}^{(4)}$ | $Z_{\mathrm{eff}}^{(6)}$ | $Z_{\mathrm{eff}}^{(8)}$ |
| 1 | 2 | 3 | 4 | 5 | 6 | 7 | 8 | 9 | 10 | 11 | 12 | 13 | 14 | 15 | 16 |
| 3 | Li | 1+ | 2.348 | 0.967 | 0.957 | 1.555 | | 22 | Ti | 2+ | 3.497 | | | 4.419 | |
| 4 | Be | 2+ | 3.348 | 1.967 | 1.957 | 2.555 | | 23 | V | 5+ | 8.139 | 7.261 | 6.059 | | |
| 5 | B | 3+ | 4.348 | 2.967 | 2.957 | 3.555 | | 23 | V | 4+ | 5.401 | | | 7.917 | 4.733 |
| 6 | C | 4+ | 5.348 | 3.967 | | 4.555 | | 23 | V | 3+ | 4.497 | | | 5.419 | |
| 7 | N | –3 | | 0.024 | 0.023 | | | 23 | V | 2+ | 3.508 | | | 5.141 | |
| 7 | N | 5+ | 6.348 | | | 5.555 | | 24 | Cr | 6+ | 9.139 | 8.261 | | | |
| 7 | N | 5+ | | 3.354 | | | | 24 | Cr | 5+ | 6.401 | | 4.389 | 8.917 | 5.733 |
| 8 | O | –2 | | 0.029 | 0.025 | 0.029 | 0.069 | 24 | Cr | 4+ | 5.497 | | | 6.419 | |
| 8 | O | 6+ | 7.348 | | | | | 24 | Cr | 3+ | 4.508 | | | 6.141 | |
| 8 | O | 6+ | | 4.354 | | | | 24 | Cr | 2+ | 3.599 | | | 4.800 | |
| 9 | F | –1 | 0.934 | 0.030 | 0.026 | 0.048 | | 24 | Cr | 2+ | | | | (hs) 5.065 | |
| 9 | F | 7+ | 8.348 | | | | | 25 | Mn | 7+ | 10.139 | 9.261 | 8.059 | | |
| 9 | F | 7+ | | 5.354 | | | | 25 | Mn | 6+ | 7.401 | | 5.389 | | |
| 11 | Na | 1+ | 3.521 | 2.252 | 1.237 | 2.574 | 3.552 | 25 | Mn | 5+ | 6.497 | | | | |
| 12 | Mg | 2+ | 4.521 | 3.252 | 2.237 | 3.574 | 4.552 | 25 | Mn | 4+ | 5.508 | | | 7.141 | |
| 13 | Al | 3+ | 5.521 | 4.252 | | 4.574 | | 25 | Mn | 3+ | 4.599 | | | 5.800 | |
| 14 | Si | 4+ | 6.521 | 5.252 | 4.237 | 5.574 | | 25 | Mn | 3+ | | | | (hs) 6.065 | |
| 14 | Si | 2+ | 4.286 | | | | | 25 | Mn | 2+ | 3.735 | | | 5.750 | |
| 15 | P | 5+ | 7.521 | 6.252 | 5.237 | | | 25 | Mn | 2+ | | | | (hs) 4.479 | |
| 15 | P | 3+ | 5.286 | | | 7.286 | | 26 | Fe | 4+ | 5.599 | | | | |
| 16 | S | –2 | | 0.044 | | 0.044 | | 26 | Fe | 3+ | 4.735 | | | 6.750 | |

Table cont.

| 1 | 2 | 3 | 4 | 5 | 6 | 7 | 8 | 9 | 10 | 11 | 12 | 13 | 14 | 15 | 16 |
|---|---|---|---|---|---|---|---|---|---|---|---|---|---|---|---|
| 16 | S | 6+ | 8.521 | 7.252 | 6.237 | | | 26 | Fe | 3+ | | | | (hs) 5.479 | |
| 16 | S | 4+ | 6.286 | | | 8.286 | | 26 | Fe | 2+ | 3.482 | | | 9.475 | |
| 16 | S | 2+ | 4.173 | | | | | 26 | Fe | 2+ | | | | (hs) 4.412 | |
| 17 | Cl | –1 | 1.373 | 0.045 | | 0.054 | | 27 | Co | 4+ | 5.735 | | | | |
| 17 | Cl | 7+ | | 8.252 | 7.237 | | | 27 | Co | 4+ | | | | (hs) 6.479 | |
| 17 | Cl | 5+ | 7.286 | | | | | 27 | Co | 3+ | 4.482 | | | 10.475 | |
| 17 | Cl | 3+ | 5.173 | | | | | 27 | Co | 3+ | | | | (hs) 5.412 | |
| 19 | K | 1+ | 4.139 | 3.261 | | 3.200 | 3.414 | 27 | Co | 2+ | 3.564 | | | 7.778 | |
| 20 | Ca | 2+ | 5.139 | 4.261 | | 4.200 | 4.414 | 28 | Ni | 4+ | 5.482 | | | 11.475 | |
| 21 | Sc | 3+ | 6.139 | 5.261 | | 5.200 | 5.414 | 28 | Ni | 3+ | 4.564 | | | 8.778 | |
| 22 | Ti | 4+ | 7.139 | 6.261 | 5.059 | 6.200 | 6.414 | 29 | Co | 2+ | | | | (hs) 7.103 | |
| 22 | Ti | 3+ | 4.401 | | | 6.917 | | 29 | Cu | 1+ | 2.879 | | | | |
| 30 | Ni | 3+ | | | | (hs) 8.103 | | 52 | Te | 6+ | 8.260 | 9.155 | | | |
| 30 | Zn | 2+ | 3.879 | 5.554 | 5.061 | 6.385 | | 52 | Te | 4+ | 7.169 | | | | |
| 31 | Ga | 3+ | 4.879 | 6.554 | 6.061 | 7.385 | | 53 | I | –1 | 1.610 | 0.066 | | 0.061 | |
| 32 | Ge | 4+ | 5.879 | 7.554 | 7.061 | 8.385 | | 53 | I | 7+ | | 10.155 | | | |
| 32 | Ge | 2+ | 4.943 | | | 5.563 | | 55 | Cs | 1+ | 4.504 | 4.513 | | 3.598 | 4.244 |
| 33 | As | 5+ | | | | 12.406 | | 56 | Ba | 2+ | 5.504 | 5.513 | | 4.598 | 5.244 |
| 33 | As | 5+ | 6.879 | 8.554 | | | | 57 | La | 3+ | 6.504 | 6.513 | | 5.598 | 6.244 |
| 33 | As | 3+ | 5.943 | | | 6.563 | | 57 | La | 2+ | 2.746 | | | | |
| 34 | Se | –2 | | 0.051 | | 0.051 | | 58 | Ce | 4+ | | 7.513 | | | 7.244 |
| 34 | Se | 6+ | | | | 13.406 | | 58 | Ce | 3+ | 3.746 | | | | |
| 34 | Se | 6+ | 7.879 | 9.554 | | | | 59 | Pr | 4+ | 4.746 | | | | |
| 34 | Se | 4+ | 6.943 | | | 7.563 | | 70 | Yb | 2+ | | | | 5.949 | 6.484 |
| 34 | Se | 2+ | 4.196 | | | | | 71 | Lu | 3+ | | | | 6.949 | 7.484 |
| 35 | Br | –1 | 1.535 | 0.052 | | 0.055 | | 72 | Hf | 4+ | | | | 7.949 | 8.484 |
| 35 | Br | 7+ | | | | 14.406 | | 73 | Ta | 5+ | | | | 8.949 | 9.484 |

Table cont.

| 1 | 2 | 3 | 4 | 5 | 6 | 7 | 8 | 9 | 10 | 11 | 12 | 13 | 14 | 15 | 16 |
|---|---|---|---|---|---|---|---|---|---|---|---|---|---|---|---|
| 35 | Br | 7+ | | 10.554 | | | | 79 | Au | 1+ | 3.756 | 4.740 | | | |
| 35 | Br | 5+ | 7.943 | | | | | 80 | Hg | 2+ | 4.756 | | 5.081 | 5.757 | 7.059 |
| 35 | Br | 3+ | 5.196 | | | | | 80 | Hg | 1+ | 3.832 | | | | |
| 37 | Rb | 1+ | 4.452 | 3.719 | | 3.104 | 3.984 | 81 | Tl | 3+ | 5.756 | 6.740 | 6.081 | 6.757 | 8.059 |
| 38 | Sr | 2+ | 5.452 | 4.719 | | 4.104 | 4.984 | 81 | Tl | 2+ | 4.832 | | | | |
| 39 | Y | 3+ | 6.452 | 5.719 | | 5.104 | 5.984 | 81 | Tl | 1+ | 4.097 | | | 5.806 | 6.115 |
| 40 | Zr | 4+ | 7.452 | 6.719 | 6.122 | 6.104 | 6.984 | 82 | Pb | 4+ | 6.756 | 7.740 | 7.081 | 7.757 | |
| 40 | Zr | 2+ | 3.724 | | | | | 82 | Pb | 2+ | 5.097 | | | 6.806 | 7.115 |
| 41 | Nb | 5+ | 8.452 | 7.719 | 7.122 | 7.104 | 7.984 | 83 | Bi | 5+ | 7.756 | 8.740 | | | |
| 41 | Nb | 3+ | 4.724 | | | | | 83 | Bi | 3+ | 6.097 | | | 7.806 | 8.115 |
| 41 | Nb | 2+ | 2.765 | | | | | 84 | Po | 4+ | | | | 8.806 | |
| 42 | Mo | 6+ | 9.452 | 8.719 | 8.122 | | | 87 | Fr | 1+ | | | | 3.955 | |
| 42 | Mo | 4+ | 5.724 | | | | | 88 | Ra | 2+ | | | | 4.955 | 5.527 |
| 42 | Mo | 3+ | 3.765 | | | | | 89 | Ac | 3+ | | | | 5.955 | 6.527 |
| 47 | Ag | 1+ | 3.260 | 4.155 | 4.511 | 5.380 | 5.894 | 90 | Th | 4+ | | | | 6.955 | 7.527 |
| 48 | Cd | 2+ | 4.260 | 5.155 | 5.511 | 6.380 | 6.894 | 91 | Pa | 5+ | | | | 7.955 | 8.527 |
| 49 | In | 3+ | 5.260 | 6.155 | 6.511 | 7.380 | 7.894 | 91 | Pa | 3+ | | | | 7.253 | |
| 50 | Sn | 4+ | 6.260 | 7.155 | 7.511 | 8.380 | 8.894 | 92 | U | 6+ | | | | 8.955 | |
| 50 | Sn | 2+ | 5.169 | | | | | 92 | U | 4+ | | | | 8.253 | |
| 51 | Sb | 5+ | 7.260 | 8.155 | | 9.380 | | 93 | Np | 5+ | | | | 9.253 | |
| 51 | Sb | 3+ | 6.169 | | | | | 94 | Pu | 6+ | | | | 10.253 | |
| 52 | Te | –2 | | 0.064 | | 0.064 | | | | | | | | | |

determined for cations of the same electronic configuration (see the detailed presentation in the preceding work [10]), hypothetical nuclear charges are assigned to anions. These charges are determined from a linear fit to the dependences of the charges on $\sqrt{E_{\mathrm{IE}}/R}$ or $1/r$ for cations of the same electronic configuration. Thus applying the screening constant to respective configurations, the effective charges of anions were calculated. In the table, the values of the effective charges of cations and anions are summarised.

It follows from the above calculations that, despite the experimental error, the values of the effective nuclear charges of ions based on ionisation enthalpies or ionic radii differentiate the ions with respect to electrostatic properties and, by means of them, different states of the ions can be described. The effective nuclear charges of isolated ions and of ions in crystal lattice are so different that they cannot be interchanged.

## 3. Conclusions

The analysis carried out in this paper demonstrates that the postulated parameter, effective nuclear charge of an ion based on ionisation enthalpies, characterises the isolated ion, whereas the effective nuclear charge based on ionic radii is the parameter characterising an ion of a given coordination number in a crystal lattice. It should be taken into account, however, that the real ion radius in a given compound is different from the tabulated value. This is why a more reliable value for determining the effective nuclear charge of ion would be the energy of the interaction of the electron with its core in crystal lattice, whose value is different from the ionisation enthalpy of the ion. The data of this type is relatively scarce.

The values of the effective nuclear charge as well as the character of the dependence of the effective charge on the formal nuclear charge indicates that it is a value that can be employed to characterise the ions with respect to their interactions.

## References

[1] MOSELEY H.G.J., Phil. Mag., 26 (1913), 1024; 27 (1914), 703.
[2] SLATER J.C., Phys. Rev., 36 (1930), 57.
[3] CLEMENTI E., RAIMONDI D.L., J. Chem. Phys., 38 (1963), 2686.
[4] BURNS G., J. Chem. Phys., 41 (1964), 1521.
[5] PAULING L., J. Am. Chem. Soc., 49 (1927), 765.
[6] ALLRED A.L., ROCHOW E.G., J. Inorg. Nuclear Chem., 5 (1958), 264.
[7] CATLOW C.R.A., MACKRODT W.C., *Computer Simulation of Solids: Lecture Notes in Physics*, 166, Springer-Verlag, Berlin, 1982.
[8] ALLEN M.P., TILDESLEY D.J., *Computer Simulation of Liquids*, Clarendon Press, Oxford, 1987.
[9] CATLOW C.R.A, *Computer Modelling in Crystalography*, Acad. Press, London, 1997.
[10] STOKŁOSA A., ZAJĘCKI J., KUREK S., Materials Sci.-Poland, 22 (2004), 17.
[11] HUHEERY J.E., KEITER E.A., KEITER R.L., *Inorganic Chemistry: Principles of Structure and Reactivity*, 4th Edition, Harper Collins, New York, 1993.

[12] *Chemical Rubber Company Handbook of Chemistry and Physics*, 79th Edition, D.R. Lide (Ed.), CRC Press, Boca Raton, Florida, USA, 1998.
[13] *Lange's Handbook of Chemistry*, 14th Edition, J.A. Dean (Ed.), McGraw-Hill, New York, 1992.
[14] WINTER M., WebElements, University of Sheffield, England, (www.webelements.com).
[15] SHANNON R.D., Acta Cryst. A32 (1976), 751.
[16] SHANNON R.D., PREWITT C.T., Acta Cryst. B 25 (1969), 925; B 26 (1970), 1046.
[17] PEARSON W.B., J. Phys. Chem. Solids, 23 (1962), 103.
[18] PHILIPS J.C., Rev. Mod. Phys., 42 (1970), 317.

*Received 10 June 2003*
*Revised 3 November 2003*

*Materials Science-Poland, Vol. 22, No. 1, 2004*

# The kinetics of photoelectric processes near interfaces of $C_{60}$/liquid crystals

O.P. BOIKO, YA. I. VERTSIMAKHA*

Institute of Physics, National Academy of Sciences of Ukraine,
Prospekt Nauki 46, 252022, Kyiv, Ukraine

The interface between vacuum deposited $C_{60}$ fullerene films and layers of nematic liquid crystals (LC), such as pentylcyanobiphenyl (5CB) or the BL055 mixture has been studied. In order to understand the processes of barrier formation at the $C_{60}$/LC interface, the kinetics of the dark current, short-circuit photocurrent and photovoltage caused by short pulses of light (~60 sec, $h\nu$ = 1.88 eV) were investigated. Initial barrier height at the $C_{60}$/LC interface and its increase caused by ion diffusion to electrodes under the action of an internal electric field or light are determined. A fast component of the short-circuit photocurrent and photovoltage was observed. This component was probably due to the presence of a partly filled acceptor-like deep electron level associated with an interaction between $C_{60}$ molecules and oxygen. The occupancy of the local states depends on molecular interactions at the interface. Their effect on the processes of ionic polarization and depolarization is discussed.

Key words: *fullerene $C_{60}$; liquid crystal; interface; photocurrent*

## 1. Introduction

Heterostructures (HS) formed by fullerenes and liquid crystals (LC), with a potential barrier at their interface, represent a new type of systems that can be applied in optical devices such as spatial light modulators [1]. To make their application possible, the mechanism of formation and properties of the potential barrier at the fullerene-LC interface has to be known.

The formation of potential barriers at interfaces between liquid crystals and organic or inorganic media, in contrast to solid-state structures, depends on the material properties of the photosensitive layer, on effects of ionic polarization and on the diffusion and deposition of ions on the electrode and photosensitive film surfaces. Due to all these factors, simple measurements of steady-state (time-averaged) characteris-

*Corresponding author, e-mail: yavertsi@iop.kiev.ua.

tics of heterostructures do not allow one to separate nor analyze these different contributions.

In order to determine the mechanism and features of potential barrier formation near the interfaces, we have studied the kinetics of dark current ($I$), short-circuit photocurrent ($I_{sc}$) and photovoltage ($V$) in HS consisting of $C_{60}$ and nematic LC (5CB and BL055) under irradiation with pulses of a red LED ($h\nu$ = 1.88 eV).

## 2. Experimental

Films of $C_{60}$ were prepared by thermal vacuum deposition ($10^{-3}$ Pa) onto glass substrates, coated with conductive (180 Ohm/cm$^2$) and transparent (80%) $SnO_2$ layers deposited by the pyrolytic technique. The substrate temperature was 300 K. The resulting $C_{60}$ layers consisted of hexagonal crystallites with Wurtzite structure in which the $C$-axis was oriented perpendicular to the substrate. The thickness of the $C_{60}$ films was controlled by an actuator and was equal to 400 nm.

Structures containing undoped LC and LC doped with $C_{60}$ with symmetrical ohmic $SnO_2$ electrodes were also prepared for comparison. Dielectric spacers ten microns thick set the thickness of the LC layers.

Measurements of the time evolution of $I$, $I_{sc}$ and $V$ were carried out with an electrometric DC amplifier, their values being recorded by a computer every 250 ms. The amplifier allows both $I_{sc}$ measurements (time constant < 1 ms) and $V$ measurements (time constant < 0.5 s) to be carried out. An external voltage was supplied with a calibrated voltage source. In order to study the processes of depolarization (trapping and recombination of charge carriers) after the illumination of the sample or after a voltage pulse (duration of ca. 60 s), the sample was connected directly to the amplifier input and the kinetics of current decay and depolarization voltage were measured.

## 3. Results and discussion

### 3.1. Dark current kinetics and C–V characteristics

It should be first noted that to diminish the influence of charge carrier injection [2] and conventional currents [3] which are usually observed for voltages higher than 3–6 V [2, 3], the measurements were carried out in the voltage range up to 2 V. The contribution of potential barriers is usually maximal in this voltage range; at higher voltages, the barriers are compensated by an external electric field.

In the control cells consisting of undoped LC and symmetrical $SnO_2$ electrodes, after an external voltage impulse $U$ is applied the dark current $I$ rises rapidly to a value $I_0$ and then, due to polarisation processes (the motion of ions to electrodes), slowly (30–60 s) approaches a steady-state value $I_s$ (Fig. 1, curve 1), as observed earlier

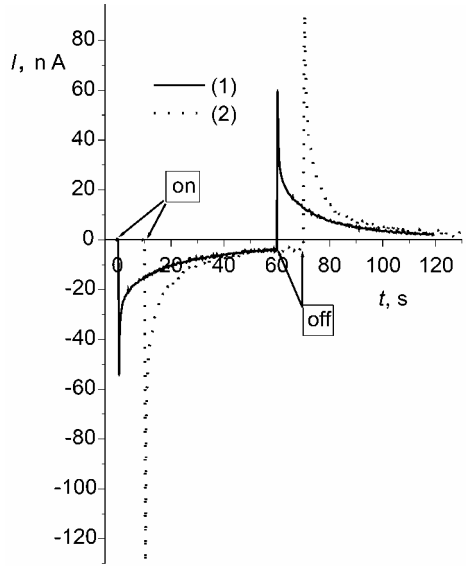


Fig. 1. Kinetics of the dark current in symmetrical 5CB LC cells (1) and $C_{60}$ solution in 5CB (<0.17 wt. %) (2) under applied voltage of 0.4 V

[4, 5]. The half-time of the decay was ca. 4 sec for cells with 5CB, and ca. 3 sec for those with BL055. The dependence of $I_0$ on voltage is practically linear for these cells (Fig. 2a, curve 1), i.e. no observable potential barriers form on the $SnO_2$/LC interfaces.

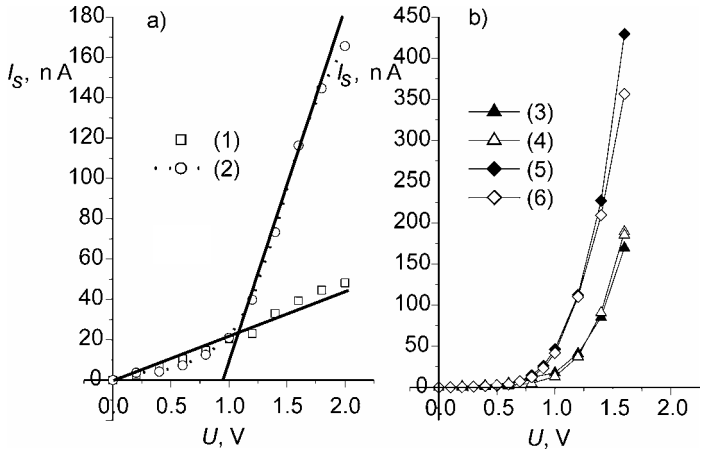


Fig. 2. Steady-state dark current–voltage characteristics in: a) symmetrical LC cells with 5CB (1) and $C_{60}$ solution in 5CB (<0.17 wt. %) (2); b) heterostructures $C_{60}$/5CB (3, 4) and $C_{60}$/BL055 (5, 6) for positive (3, 5) and negative (4, 6) polarity on LC

The dark current kinetics of $C_{60}$/LC HS is generally similar to the kinetics of LC cells with ohmic $SnO_2$ electrodes, although both the initial ($I_0$) and steady-state ($I_s$)

currents, and also their relaxation times, depend on the value of $U$ and its polarity. For voltages up to 1.5 V of both polarities the dependence $I_0(U)$ has a poorly expressed exponential character, being almost symmetrical (weakly depending on the polarity of $U$). It is similar to characteristics of two counter-connected equivalent diodes with a large series resistance $r_s$. At voltages between 1.5 and 2.0 V, $I_0(U)$ becomes almost linear, allowing $r_s$ to be estimated. For the structures studied, $r_s \cong$ (10–40) MOhm. An extrapolation of the linear part of $I_0(U)$ gives a cut-off voltage of 0.35± 0.05 V for HS with BL055 and ca. 0.2 V for HS with 5CB. One may thus estimate the initial band bending (initial barrier height, $Y_0$) to be in the range of (0.2–0.4) eV.

The voltage dependences of steady-state current ($I_s$) are clearly exponential in HS of both 5CB and BL055 (Fig. 2b). Extrapolation of the linear parts of $I_s(U)$ dependences yields cut-off voltages of 1.03 ('+' on LC) and 1.07 V ('–' on LC) for $C_{60}$/BL055 HS, and 1.10 and 1.15 V for $C_{60}$/5CB HS. The obtained cut-off values are probably approximately equal to the sum of the barrier heights in these HS. This is equal to a first approximation to the sum of the initial barrier height in the darkness before supplying external voltage $Y_0$ and an additional band bending $Y_p$. The latter are formed due to the diffusion and adsorption of ions on the electrodes, usually called as the polarization process [4]. The total barrier in $C_{60}$/LC is more than 3 times higher than that obtained for CdSSe/BL055 HS [5].

Most surprising for us was the fact that $I_s(U)$ was almost symmetrical, although the $C_{60}$ layer was deposited onto one electrode only. It was thus supposed that $I_s(U)$ would be asymmetrical, as earlier observed for CdSSe/LC HS [5]. An analysis of possible reasons for this feature has shown that it was most probably caused by a poor solubility of $C_{60}$ in LC, which we were unable to observe earlier. After the cell preparation, a part of the $C_{60}$ molecules diffused from the film to the LC and then precipitated on the opposite 'clean' $SnO_2$ electrode (on which we did not deposit any $C_{60}$ layer). Naturally, the precipitation process would occur only when there is no quasi-stationary equilibrium. Before this equilibrium established, part of the molecules in the LC layer formed ions or charged complexes consisting of $C_{60}$ and LC molecules. This model seems to be confirmed by an increase of $I_0$ (in the cells containing LC doped with 0.17 wt. % of $C_{60}$ it is 2.4 times larger than in those containing undoped LC – cf. Fig. 1, curve 1).

Since $C_{60}$ molecules are strong acceptors (trap centres for electrons) [6], it is reasonable to assume that the concentration of negative ions will increase in the LC layer. Therefore, potential barriers of practically identical height but of opposite polarities are formed at both electrodes of HS.

To check experimentally our hypothesis, we measured $I_s(U)$ characteristics in a cell with two symmetrical $SnO_2$ electrodes, between which LC doped with <0.17 wt. % of $C_{60}$ (maximum solubility at 300 K) was placed. The measured $I_s(U)$ dependence for such a cell, presented in Fig. 2a (curve 2), is almost symmetrical and has an exponential character, which confirms our suggestion. The cut-off voltage for this dependence $Y \cong 0.95$ V, i.e. is only 8–15% smaller than the cut-off for the HS in which the $C_{60}$

layer is deposited by thermal vacuum evaporation. The difference may be caused by differences between the structures of a layer deposited by vacuum evaporation and formed as a result of $C_{60}$ precipitation onto the surface of $SnO_2$ electrodes.

## 4. Photovoltaic properties

The main attention in the present study was given to measurements of current kinetics, since the time constant of the measuring device is small in this mode (<1 ms) and transitional processes can be recorded more clearly.

A typical $I_{sc}$ kinetics measured in a $C_{60}$/LC HS under the excitation with a pulse of 'red' LED ($h\nu$ = 1.88 eV) is shown in Fig. 3a, b. $I_{sc}$ kinetics for CdSSe/BL055 HS are also shown for comparison (Fig. 3c).

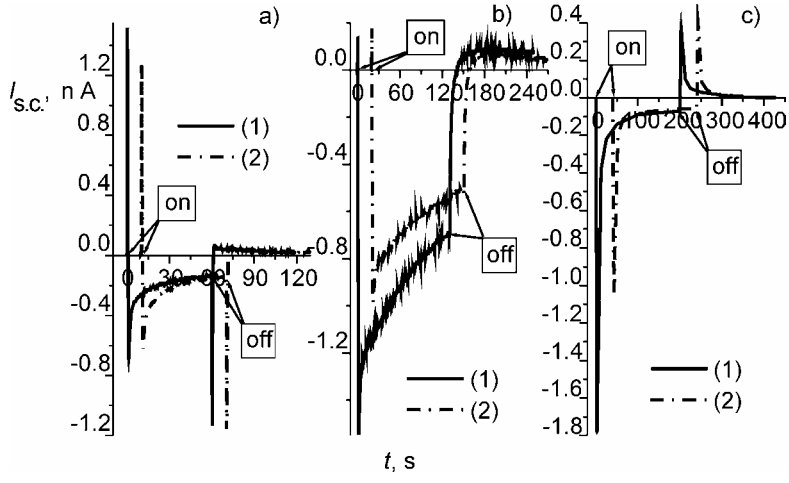


Fig. 3. Kinetics of the photocurrent in heterostructures $C_{60}$/BL055 (a), $C_{60}$/5CB (b) and CdSSe/BL055 (c) under illumination ($h\nu$ = 1.88 eV) through LC (1), $C_{60}$ or CdSSe (2)

It can be seen that the presence of an $I_{sc}$ peak with a '–' on the illuminated surface (independent of the illumination direction) and the following slow decrease with the decay time of 20 sec (for HS with BL055) and 100 sec (for HS with 5CB) is common to all these HS. We were not able to record $I_{sc}$ for the structure with symmetrical $SnO_2$ electrodes, since LC does not absorb this light.

The peculiarity of $C_{60}$/LC is the presence of a fast short circuit component of opposite sign ($I_{scb}$). The rise and fall times of $I_{scb}$ are both approximately 1 sec. The peak $I_{scb}$ value for $C_{60}$/BL055 HS (Fig. 3a) is almost 5 times greater than for $C_{60}$/5CB HS (Fig. 3b), i.e. $I_{scb}$ strongly depends on the LC material.

The presence of $I_{scb}$ in $C_{60}$/LC HS may be caused by the formation of acceptor-like deep electron levels (filled in the darkness) in $C_{60}$ (near the $C_{60}$/LC or $SnO_2$/$C_{60}$ interface), which according to [6] (Fig. 4) are situated at 0.8 eV under the conduction band

and are probably due to interactions of $C_{60}$ molecules with oxygen. Upon illuminating the $C_{60}$ layer carriers are released from these centres. Consequently the concentration of trapped electrons decreases and therefore the $I_{scb}$ signal decreases. A decrease in the occupancy of this impurity level will naturally cause a shift of the quasi-Fermi level resulting in a fast increase of $Y_0$. Naturally, the position of the Fermi level at the $C_{60}$/LC interface will depend on the interaction of LC with the $C_{60}$ film surface and even its small shift will strongly change the occupancy of this level and consequently the peak value of $I_{scb}$. This may explain the smaller value of $I_{scb}$ in $C_{60}$/5CB HS (Fig. 3b). This acceptor-like level is probably localized near the $C_{60}$/LC interface, since oxygen is adsorbed on the film surface after its preparation. Consequently, the concentration of adsorbed oxygen molecules and their complexes with $C_{60}$ molecules will be larger on the free surface of $C_{60}$ film.

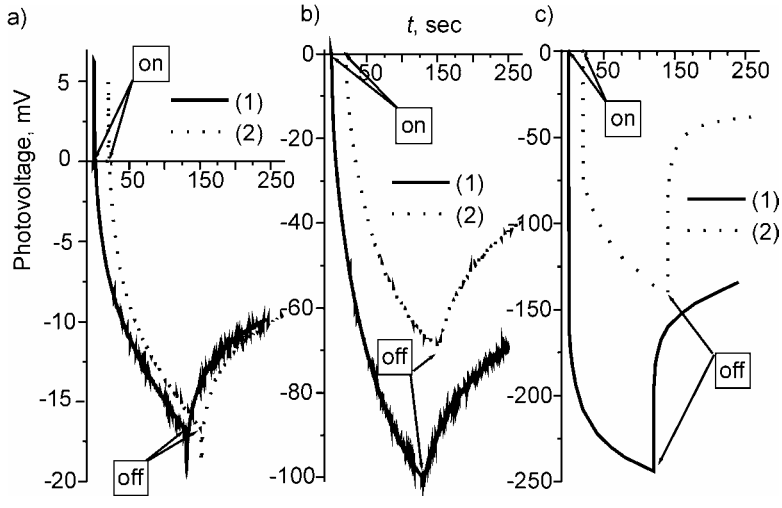


Fig. 4. Kinetics of the photovoltage in heterostructures $C_{60}$/BL055 (a), $C_{60}$/5CB (b) and CdSSe/BL055 (c) under illumination ($h\nu$ = 1.91 eV) through LC (1), $C_{60}$ or CdSSe (2)

To verify whether such an impurity level is indeed formed in our structures, we carried out measurements of the surface conductivity of $C_{60}$ layers in vacuum and in the ambient atmosphere. The specific resistance of the layers in the darkness in vacuum is of the order of $10^{10}$ Ohm·cm. In the air, due to oxygen adsorption on the free surface of films, their resistance slowly increases by more than 2 orders of magnitude, and the photocurrent decreases, in agreement with the literature data [6]. After air is pumped out, only a partial reversibility of dark resistance and photocurrent is observed, i.e. deep trapping centres (probably charge transfer complexes between $C_{60}$ molecules and oxygen) remain. This result confirms that the formation of acceptor-like levels acting as deep trapping centres on the surface of the investigated $C_{60}$ films can indeed take place.

As was shown in the previous sections, it follows from the analysis of $I(U)$ dependences that blocking barriers are formed near both electrodes in the studied $C_{60}$/LC HS and the measured structures are similar to two counter-connected diodes. In this case, $I_{sc}$ recorded by the meter is:

$$I_{sc} = A(d_1 - \gamma_1 d_2) \tag{1}$$

where $A$ is a constant proportional to the quantum efficiency of the charge carrier photogeneration and to absorbance (practically equal for deposited and precipitated layers), $d_1$ is the thickness of the illuminated layer, $d_2$ – the thickness of the layer near the opposite electrode, and $\gamma_1$ – the coefficient of the decrease in light intensity on the opposite electrode due to its absorption in the first layer and scattering in the LC layer.

Analogously, the measured value under the illumination of the opposite electrode is:

$$I_{sc}^{*} = A(d_2 - \gamma_1 d_1) \tag{2}$$

We do not know the thickness of the precipitated layer formed due to diffusion from the LC layer onto the 'clean' electrode. To estimate it, we have measured $I_{sc}$ for the cell with two symmetrical $SnO_2$ electrodes, between which LC doped with <0.17 wt. % of $C_{60}$ was placed, and for which the $C$–$V$ characteristic is exponential (Fig. 1b). The value of $I_{sc}$ in these structures was more than two orders smaller than that for HS. This is evidence that $d_2 << d_1$ and that the influence of the precipitated layer in $I_{sc}$ formation can be neglected during the further analysis of photovoltaic properties.

A slow decrease of $I_{sc}$ is observed after reaching the peak value (Fig. 3). A similar decrease is observed in the kinetics of dark current (Fig. 1). The decrease of both $I_{sc}$ and dark current can be explained by the diffusion of LC ions towards the electrodes and their separation by the intrinsic field of the initial barrier [4, 5]. It is obvious that the concentration of ions due to their transport to the electrodes will decrease and simultaneously the additional intrinsic electric field near the electrodes will increase. The decrease of ion concentration should lead to an increase in the differential resistance of the structure and a decrease of $I_{sc}$. To explain $I_s(U)$ dependences, we supposed that the barrier height $Y$ and internal electric field increase due to ion diffusion, which in turn should lead to an increase in $I_{sc}$. From Fig. 1 it is clear that only a decrease in $I_{sc}$ is observed in the studied HS, i.e. the main contribution to the process comes from an increase in structure resistance. Because of this, determining the direction of the internal electric field is impossible from $I_{sc}$ kinetics alone.

Since the value of $V$ does not depend on structure resistance, we have carried out a measurement of its kinetics to solve this problem (Fig. 4).

It can be seen that in both types of $C_{60}$/LC HS quasi-steady-state value of $V$ has the same sign (negative at the illuminated surface). A slow increase in $V$ is observed in all structures after reaching the maximal value of $I_{sc}$, i.e. the directions of the initial and additional electric fields (barriers) are the same.

It is possible to estimate the ratio of the heights of the initial barrier and an additional one, created by ion diffusion ($Y_0/Y_p$) by measuring the ratio of fast and slow components of $V$, built up under the illumination through LC layer. The $Y_p/Y_0$ ratio is 0.7–0.8 for $C_{60}$/LC HS (for comparison, it amounts to 0.5 for CdSSe/BL055 HS), being in good agreement with the data obtained from an analysis of the dark current –voltage characteristics. This confirms that the contribution of ion diffusion is dominant in the formation of internal electric fields in the studied HS.

## 5. Depolarization processes

After the sample has been biased with a voltage, a drift of ions initially concentrated near the electrodes towards the middle of the LC layer is initiated. Ions partially recombine with ions of opposite charge drifting in the opposite direction. Due to this, a current in the opposite direction arises (the depolarization current, $I_d$ [4]) with a time constant $\tau_d$ close to, but not equal to, the time constant of polarization $\tau_p$. Naturally, the ratio of the charge that is released during the depolarization ($Q_d$) to that trapped during the polarization ($Q_p$) cannot exceed unity, although this does not mean that the peak value of $I_d$ cannot be larger than the peak value of the depolarization current $I_p = (I_0 - I_s)$. On the contrary, if $\tau_d < \tau_p$ (as in the case, e.g., of CdSSe/LC HS) then $I_d/I_p$ can be > 1. Therefore, the efficiency of recombination can be correctly estimated if the ratio $Q_d/ Q_p$ is known.

Typical kinetics of dark current are shown in Fig. 1. In symmetrical LC structures undoped and doped with $C_{60}$, both $I_d$ and $Q_d$ are practically independent of the polarity and are proportional to $U$ at $U < 1$ V. They also tend to saturate at higher voltages, while $Q_p$ practically linearly depends on $U$. $I_d$ and $Q_d$ also tend to saturate at $U$ >1.2 V ($eU > Y$), while $Q_p$ superlinearly depends on $U$ at these voltages. Due to this, the ratios of $Q_d/Q_p$ and $I_d/I_p$ markedly decrease in all structures when $U$ increases in the range $U > 1$ V. Therefore, the efficiencies of polarization and depolarization in the different studied structures can be correctly compared using parameters obtained at $U = 1$ V only. They are presented in Table 1.

It can be deduced from the values of the $Q_d/Q_p$ ratio that 80% of the ions recombine and/or are trapped in deep capture centres during polarization in LC structures with ohmic electrodes and only 20% of them reach the opposite electrode in these structures. Even higher fractions of ions (c.a. 90%) recombine or are trapped by deep capture centres in HS. An observed rise in the efficiency of recombination and trapping of ions in HS can be explained by the presence of intrinsic electric fields.

Depolarization processes have also been observed in HS after the illumination was switched off, as is well seen in Fig. 3. The decay of the depolarisation current in this case (hereafter denoted $I_{sd}$) is similar to that of $I_d$ after switching off the voltage. Thus one can formally use the same formalism to characterize the kinetic processes. In the following, we shall employ the same parameters marked additionally with the subscript s.

Table 1. Parameters characterizing processes of polarization and depolarization for LC cell and HS under 1V voltage pulse in dark

| Parameters | Structure | | | | | | | | |
|---|---|---|---|---|---|---|---|---|---|
| | BL055 | CdSSe/BL055 | | $C_{60}$/BL055 | | % 5CB | 5CB + 0.1% $C_{60}$ | $C_{60}$/5CB | |
| $U$ sign | ± | +LC | –LC | +LC | –LC | ± | ± | +LC | –LC |
| $I_0$, nA | 4.67 | 8.40 | 5.27 | 290 | 284 | 150.8 | 190 | 62 | 57 |
| $I_s/I_0$ | 0.27 | 0.11 | 0.03 | 0.16 | 0.15 | 0.09 | 0.08 | 0.28 | 0.23 |
| $(I_0 - I_s)/I_0$ | 0.73 | 0.89 | 0.97 | 0.84 | 0.85 | 0.91 | 0.92 | 0.71 | 0.77 |
| $Q_p/Q_0$ | 0.96 | 0.78 | 0.90 | 0.76 | 0.81 | 0.84 | 0.81 | 0.65 | 0.72 |
| $I_d/(I_0 - I_s)$ | 0.59 | 0.97 | 1.10 | 1.16 | 1.23 | 0.56 | 1.09 | 1.12 | 0.99 |
| $Q_d/Q_p$ | 0.20 | 0.07 | 0.07 | 0.05 | 0.05 | 0.14 | 0.17 | 0.11 | 0.08 |

It should be noted that the efficiency of depolarization $I_{scb}$ (current of electrons detrapped from the surface level upon illumination) and $I_{sc}$ (which is mainly ionic current) differ greatly. 85–90% of the photoexcited electrons in $C_{60}$/BL055 HS are retrapped probably by the same centres (Fig. 3a). The parameters obtained for ion depolarization are presented in Table 2.

Table 2. Parameters characterizing processes of polarization and depolarization for HS under illumination with a red LED ($h\nu = 1.88$ eV)

| Structure | CdSSe/BL055 | | $C_{60}$/ BL055 | | $C_{60}$/ 5CB | |
|---|---|---|---|---|---|---|
| Illuminated side | LC | $SnO_2$ | LC | $SnO_2$ | LC | $SnO_2$ |
| $I_{s0_2}$, nA | 1.78 | 0.10 | 690 | 624 | 1541 | 983 |
| $I_{ss}/I_{s0_2}$ | 0.04 | 0.06 | 0.19 | 0.22 | 0.45 | 0.51 |
| $k_p = (I_{s0} - I_{ss})/I_{s0}$ | 0.96 | 0.94 | 0.81 | 0.78 | 0.55 | 0.49 |
| $Q_p/Q_0$ | 0.90 | 0.95 | 0.72 | 0.66 | 0.40 | 0.34 |
| $k_d = I_{d0}/(I_{s0} - I_{ss})$ | 0.22 | 0.43 | 0.12 | 0.14 | 0.10 | 0.14 |
| $Q_d/Q_p$ | 0.019 | 0.026 | 0.06 | 0.08 | 0.105 | 0.14 |

A comparison of ion polarization and depolarization parameters in LC structures and in HS under the action of electric field or light impulses (Tables 1 and 2) reveals that in the latter case, about 90% of ions recombine or become trapped during the depolarization in HS. However, the rate of depolarization in this case is noticeably smaller ($\tau_{ds} > \tau_d$). This effect can be due to the diminution of the capture efficiency of nonequilibrium carriers by trapping centres. This probably stipulates the attenuation of polarization processes (decrease of $Q_p/Q_0$ ratios) upon excitation by light.

## 6. Conclusions

The initial bands bending of ca. 0.35 eV exists in $C_{60}$/LC HS. This value increases up to (1.0–1.1) eV due to ion transport to electrodes after applying an external field. The presence of even a small amount of $C_{60}$, whose solubility in LC is of the order of

ca. 0.1 wt. % in the studied structures, leads to the diffusion of $C_{60}$ from the deposited layer in LC and their precipitation on the opposite $SnO_2$ electrode. This results in the formation of almost symmetrical HS after cell preparation with almost the same potential barrier heights near both electrodes. Hence the dependences of current on the external voltage in the darkness become exponential and almost symmetrical, and ion concentration in LC increases.

Another peculiarity of $C_{60}$/LC HS is the appearance of a fast component in the short-circuit photocurrent and photovoltage, caused by a change in the occupancy of acceptor-like deep electron levels, whose presence is due to interactions of $C_{60}$ molecules with oxygen. The occupancy depends on the interaction of LC molecules with $C_{60}$ molecules near the interface.

80% of the charges recombine and/or become trapped in deep levels during the process of depolarization in LC structures with ohmic contacts. The efficiency of this process increases to 90% in HS, practically independently of the excitation method (illumination or external electric field).

## References

[1] MUL'NIKOV V.S., Optical Journal, 7 (1993), 41 (in Russian).
[2] JANUSZKO A., MINIEWICZ A., Adv. Mat. Optics Electronics, 6 (1996), 272.
[3] KAPUSTIN A.P., *Experimental studies of liquid crystals*, Moscow, Nauka, 1978 (in Russian).
[4] GRITSENKO N.I., MOSHEL N.V., Ukr. Phys. J., 25 (1980), 1830.
[5] VERTSIMAKHA Ya.I., BOIKO O.P., Mol. Cryst. Liq. Cryst., 361 (2001), 165.
[6] MAKAROVA T.L., Fiz. Tekh. Poluprov., 35 (2001), 257.

*Received 18 February 2003*
*Revised 23 September 2003*

*Materials Science-Poland, Vol. 22, No. 1, 2004*

# Pamoate intercalated Zn-Al layered double hydroxide for the formation of layered organic-inorganic intercalate

M. Z. HUSSEIN*, Z. B. JUBRI, Z. ZAINAL, A. H. YAHYA

Multifunctional Nanomaterials for Industrial Application (MULIA) Research Group,
Department of Chemistry, University Putra Malaysia, 43400 Serdang, Selangor, Malaysia

A layered organic-inorganic intercalate was prepared by the self-assembly technique using pamoate (PA) as an organic guest in the Zn-Al layered double hydroxide inorganic host (ZAPAN). Various concentrations of PA, ranging from 0.01 to 0.04 M, were used to prepare the intercalated compound with a constant 4:1 ratio of Zn:Al in the mother liquor. The concentration of PA of 0.02 M at pH 7 was found to give a well-ordered nanolayered organic-inorganic hybrid structure. As a result of successful intercalation of PA anion into the Zn-Al inorganic layered double hydroxide (LDH), the expansion of interlayer spacing to 18 Å was observed in the PXRD diffractogram of the intercalated compound, compared to 9 Å for the Zn-Al LDH with nitrate as the counter anion (ZANIL). FTIR study shows that the intercalated compound resembled the spectra of PA and ZANIL, thus indicating the presence of both functional groups in ZAPAN. It was also found that the BET surface area increased from 6 $m^2/g$ to 90 $m^2/g$ for ZANIL and ZAPAN, respectively. The pore texture of the resulting materials was also changed as the result of the intercalation and the expansion of the basal spacing together with pore formation between the crystallite during the formation of the resulting layered intercalated compound.

Key words: *organic-inorganic intercalate; pamoic acid; layered double hydroxide; hydrotalcite*

## 1. Introduction

Intercalated compounds of organic-inorganic hybrid type have been extensively studied for some time and it was shown that the resulting properties can be tailored to a specific requirement needed to serve specific purposes. This type or materials can be synthesised by employing a variety of interactions found within the organic and inorganic chemistry, to create a composite with some enhanced property relative to

*Corresponding author, e-mail: mzobir@fsas.upm.edu.my.

that achievable by its counterpart alone, or to combine useful properties of the two within a single material [1].

In the syntheses of organic-inorganic materials of hybrid intercalate type, layered double hydroxides (LDHs) can be chosen as one of the inorganic hosts. LDHs has a general formula $[[M^{2+}_{1-x}M^{3+}_{x}(OH)_2]^{x+}(A^{n-})_{x/n}\cdot mH_2O$, where $M^{2+}$ and $M^{3+}$ are divalent and trivalent cations, respectively, $x$ is the $M^{3+}/(M^{2+}+M^{3+})$ ratio and $A^{n-}$ is an interlayer anion. Such $A^{n-}$ anions may be polymers [2, 3], organic dyes [4], surfactants [5, 6] or organic acids [7].

Previous work on the intercalation of various organic molecules into the hydroxide layers have been carried out for various purposes and applications. For example, the replacement of inorganic anions in LDHs with organic species such as long-chain surfactants resulted in a modified organo-LDHs with surfaces of hydrophobic properties. Anionic surfactants such as octylsulfate, sodium dodecylsulfate, sodium 4-octylbenzenesulfonate and sodium dodecylbenzenesulfonate were used. The resulting organo-LDHs were studied by evaluating their abilities to adsorptively remove 1,2,4-trichlorobenzene and 1,1,1-trichloroetane from aqueous solutions [5]. Another example is the intercalation of ibuprofen, α-methyl-4-(2-methylpropyl)benzene-acetic acid which is an anti-inflammatory drug into Zn-Al LDH, in order to study the controlled release property of the former from the controlled release formulation [8]. This is particularly useful for medical and agricultural purposes [7].

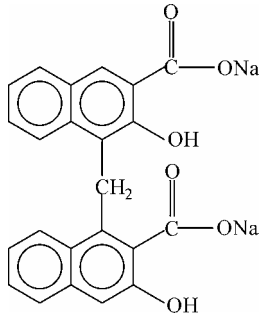

Fig. 1. The molecular formula of pamoate salt

Layered organic-inorganic intercalates can be prepared by propping the LDH inorganic layers apart followed by insertion of the organic moiety. This can be done directly or indirectly. In the direct method or the so-called spontaneous self-assembly method, formation of the resulting material can be accomplished by co-precipitation of cations in a basic aqueous solution in the presence of the anions to be intercalated in the interlayer, followed by ageing processes. In the indirect method, the preparing of the host is followed by its modification or further treatment and finally embedding of anions into the layers [6, 9]. For both methods, physicochemical and structural, properties of the resulting materials depend on the precipitation pH, temperature, ageing time, washing and drying conditions.

In this paper, we report on the intercalation of the anions of 1,1′-methylene-bis-[2-hydroxy-3-naphthoic acid] (pamoic acid, pamoate) into the Zn-Al LDH to form a new organic-inorganic hybrid intercalated material. The molecular structure of the pamoate salt ($C_{23}H_{14}O_6Na_2$) is shown in Fig. 1. It is the salt of an aromatic dicarboxylic acid, used as a means of masking unpleasant tastes or prolonged therapeutic action by forming slightly soluble salts with certain basic drugs [10]. A derivative of pamoic acid, pyrantel pamoate, is used for the treatment of infestation of gastrointestinal parasite [11].

## 2. Experimental

All chemicals used in this synthesis were obtained from various chemical suppliers and used without any further purification. All solutions were prepared using deionized water.

The synthesis of the intercalated compound, ZAPAN, was done by the spontaneous self-assembly method. A mother liquor containing $Zn^{2+}$ and $Al^{3+}$ cations with Zn/Al initial ratio $R_i$ = 4 and PA was prepared. pH was adjusted to about 7. The concentration of PA was from 0.01 M to 0.04 M and the reaction was carried out under nitrogen atmosphere. The solution was aged for 18 h in an oil bath shaker at 70 °C. The resulting precipitate was centrifuged, thoroughly washed and dried in an oven at 70 °C for 3 days and kept in a sample bottle for further use and characterizations. A similar method was adopted for the preparation of Zn-Al LDH with nitrate as the intergallery anion (ZANIL) by omitting the addition of PA solution in the mother liquor.

Powder X-ray diffraction (PXRD) patterns of the samples were obtained with a Shimadzu Diffractometer XRD-6000, using filtered $CuK_\alpha$ radiation. FTIR spectra were recorded by a Perkin-Elmer 1750 Spectrophotometer. KBr pellet containing a 1% sample was used to obtain the FTIR spectra. The surface morphology of the samples was observed by a scanning electron microscope (SEM), using JOEL JSM-6400. A CHNS analyser, model EA 1108 of Finons Instruments, was used for CHNS analyses. The percentage of PA in ZAPAN was established by means of a UV-visible technique using a Perkin-Elmer UV-visible Spectrophotometer model Lambda 20. The Zn/Al ratio of the resulting ZAPAN was determined by an inductively coupled plasma emission spectrometry (ICP-ES) with a Labtest Equipment Model 710 Plasmascan sequential emission spectrometer.

Surface characterization of the materials was carried out by the nitrogen gas adsorption-desorption technique at 77 K using a Micromeritics ASAP 2000. Samples were degassed in an evacuated-heated chamber at 120 °C, overnight.

## 3. Results and discussion

### 3.1. Powder X-ray diffraction

Figures 2a–f show PXRD patterns of the LDH, ZANIL and its intercalated compound, ZAPAN, prepared using various concentrations of PA from 0.01 M to 0.04 M. As shown in Fig. 2a, the basal spacing for ZANIL with nitrate as the interlamella anion is 9 Å which is similar to the value reported previously [12].

The PXRD pattern for ZAPAN is shown in Fig. 2c with basal spacing of 18 Å. The expansion of basal spacing from ZANIL to ZAPAN is due to the inclusion of PA into the LDH lamella with an orientation that warrants the expansion of the LDH lamella. This can only be achieved if suitable concentration of PA is available in the

mother liquor, under the experimental conditions stated earlier. Noteworthy also that for ZAPAN prepared by using 0.03 M and 0.04 M PA, a number of peaks which are characteristic of PA phase were detected. This might be due to the unintercalated PA, which was adsorbed onto the surface of ZAPAN due to a high concentration of PA being used in the synthesis.

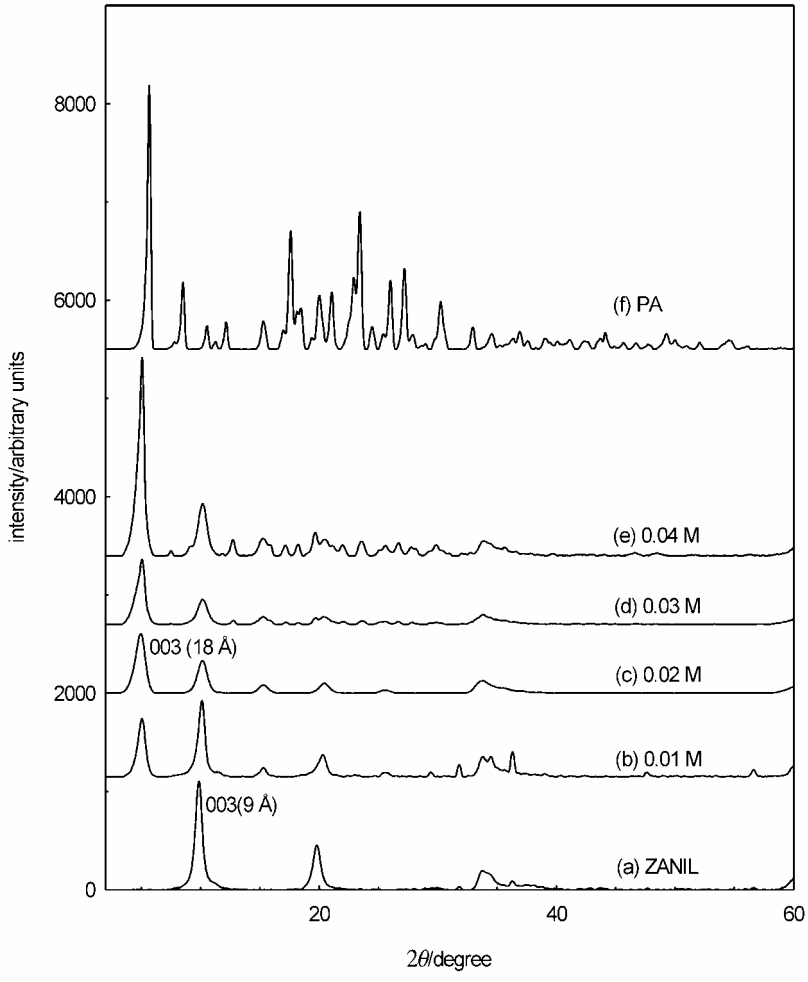


Fig. 2. PXRD pattern for ZANIL and its intercalated compound with PA (ZAPAN) prepared at various concentrations of PA

For ZAPAN prepared using 0.01 M PA, ZnO phase was also detected. ZAPAN prepared by using 0.02 M PA produced sharp, symmetrical and intense peaks, especially for the (003) peak, and relatively pure intercalated compound was obtained at this concentration. As a result of successful intercalation of PA, ZAPAN prepared from 0.02 M PA was subsequently used for further characterizations.

### 3.2. FTIR spectroscopy

In figure 3, the FTIR spectra for PA, ZANIL and ZAPAN are shown. The FTIR spectrum for ZANIL (Fig. 3a) shows a broad absorption band centred at around 3438 $cm^{-1}$ which is due to the presence of OH stretching modes of the hydroxyl group

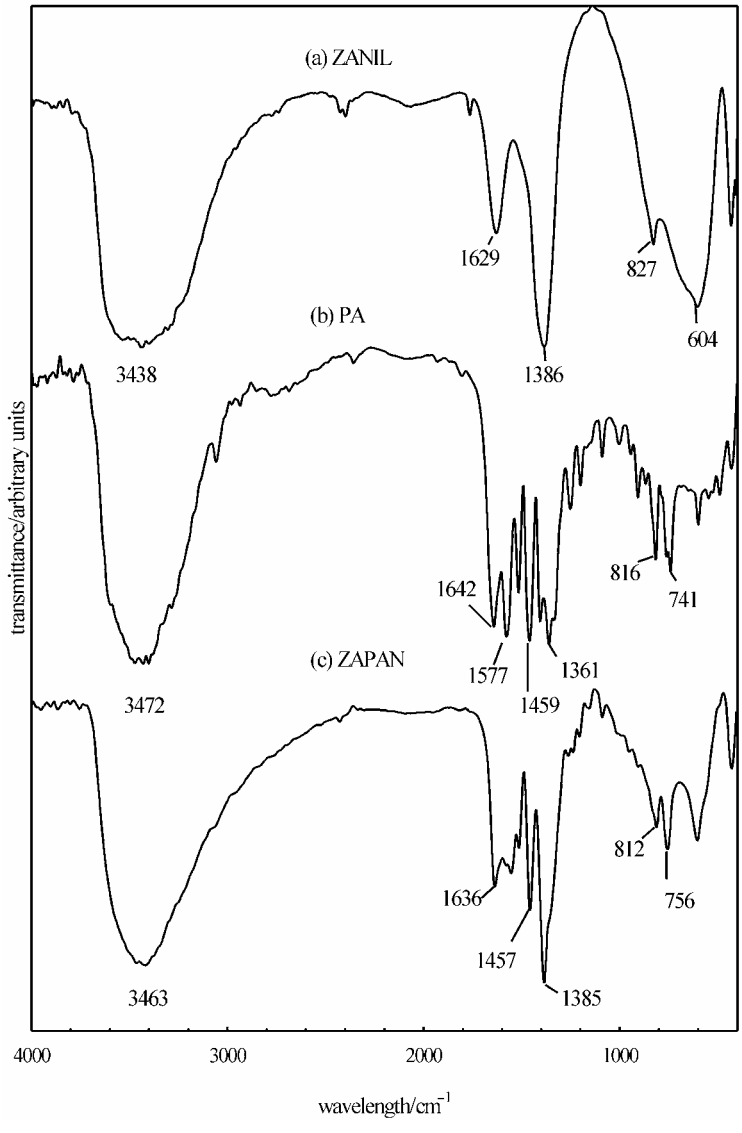


Fig. 3. FTIR spectra for: a) ZANIL, b) PA, c) ZAPAN

of LDH and/or physically adsorbed water molecules. The band at 1629 $cm^{-1}$ is due to $\nu_{H–O–H}$ bending vibrations. A sharp and very intense band located at approximately

1386 $cm^{-1}$ is attributed to the $\nu_3$ ( $NO_3^-$ ) vibration [13]. Another two bands at 604 $cm^{-1}$ and 432 $cm^{-1}$ can be attributed to the Al–OH and Zn–Al–OH bending vibrations, respectively [6].

Figure 3b shows the FTIR spectrum of PA displaying a broad band at 3472 $cm^{-1}$, which is attributed to the OH stretching vibration. Strong bands at 1577 and 1361 $cm^{-1}$ are due to the antisymmetric and symmetric stretching modes of –COO, respectively [8]. The bands at 1516 and 1642 $cm^{-1}$ are attributed to the stretching vibrations of aromatic rings, C=C, and the other sharp intense band at 1459 $cm^{-1}$ is due to $CH_2$ scissoring mode. Strong bands near 741–816 $cm^{-1}$ can be attributed to the presence of phenyl ring substitution [14].

The FTIR spectrum of ZAPAN synthesized by using 0.02 M PA is shown in Fig. 3c. As expected, the spectrum resembles a mixture of both the spectra of PA and ZANIL, indicating that both functional groups of PA and ZANIL are simultaneously present in ZAPAN and confirm the intercalation of PA in the interlamella of ZANIL.

### 3.3. Organic-inorganic composition

The organic and inorganic composition of ZANIL and ZAPAN is compared in the table. The ratios of Zn/Al ($R_f$) in ZANIL and ZAPAN are 3.0 and 3.3, respectively. Compared to 4.0 for the initial ratio in the mother liquor, a slightly lower $R_f$ value than $R_{initial}$ indicates that not all $Zn^{2+}$ ions in the mother liquor were used for the formation of positively charged layers of the inorganic double hydroxide during the formation of ZANIL or ZAPAN.

Table. Physicochemical properties of ZANIL and ZAPAN

| Salt | [a]$R_f$ | *C* wt.% | *PA* wt.% | *N* wt.% | BET surface area ($m^2 \cdot g^{-1}$) | BJH desorption pore volume ($cm^{-3} \cdot g^{-1}$) | BJH average pore diameter (Å) |
|---|---|---|---|---|---|---|---|
| ZANIL | 3.0 | – | – | 3.8 | 6 | 0.028 | 87 |
| ZAPAN | 3.3 | 24.1 | 44.2 | 0.8 | 90 | 0.342 | 115 |

[a]$R_f$ = final ratio.

The CHNS analysis shows that ZAPAN contained 24.1% of carbon which indicated that PA was successfully intercalated in the interlayer lamella of ZAPAN. The CHNS analysis also shows that ZANIL contained 3.8% of nitrogen. This is in agreement with the presence of a strong, sharp band at about 1386 $cm^{-1}$ in the FTIR spectrum of ZANIL in Fig. 3a, which might be due to the presence of nitrate. As shown in the table, the percentage of PA intercalated into the interlayer of ZAPAN is 44.2% measured by an UV-visible spectrophotometer.

### 3.4. Thermal analysis

The results of thermogravimetric analyses (TGA) and differential TGA (DTG) of PA, ZANIL and ZAPAN are shown in Fig. 4. ZANIL, which is a hydrotalcite-like

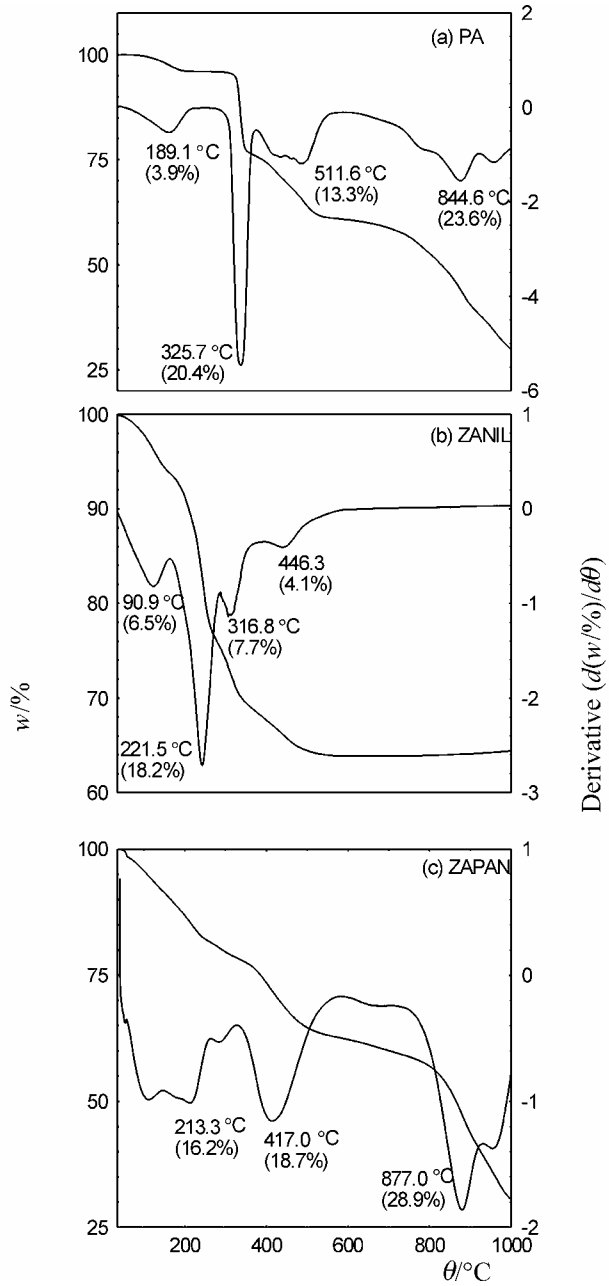


Fig. 4. TGA and DTG thermograms for: a) PA, b) ZANIL, c) ZAPAN

compound, shows four major stages of the weight loss process occurring at the temperature maxima of 90.9, 221.5, 316.8 °C and 446.3 ºC, with weight losses of 6.5, 18.2, 7.7 and 4.1%, respectively. The first weight loss corresponds to the removal of water physisorbed on the external surface of the particles. The second weight loss is attributed to strongly held water molecules [15]. The third and fourth weight losses are almost completed at 450 ºC and correspond to removal of hydroxyl groups from the brucite-like layers and the removal of interlayer anions. The DTG curves for PA exhibit four major stages of weight loss process at the temperature maxima of 189.1 ºC (3.9%), 325.7 ºC (20.4%), 511.6 ºC (13.3%) and 844.6 ºC (23.6%). The TGA shows the first weight loss below 200 ºC which is ascribed generally to the loss of physically adsorbed water. The second weight loss can be attributed to the evolution of carbon dioxide and water by thermal decomposition of the organic molecules. Decomposition at higher temperature (above 400 ºC) is due to a non-vaporizable nature of the organic anions [16]. The DTG curves of ZAPAN show three major stages of weight loss. The first weight loss is due to the removal of water physisorbed on the external surface of the powder particles. The second one should be due to simultaneous loss of carbonate and dehydroxylation of the brucite-like layer and the third weight loss above 800 ºC corresponds to the decomposition of the organic moiety in the interlayer lamella of the nanohybrid material [17]. The percent weight losses are 16.2, 18.7 and 28.9% at 213.3, 417 and 877 ºC, respectively.

Comparison of Figs. 4a and 4c shows that the temperature maximum for the decomposition of the organic moiety is higher in the latter which proves that PA intercalated inside the LDH is thermally more stable than its original form as a sodium salt.

### 3.5. Surface properties

*Isotherm, surface area and pore size distribution.* In order to study the effect of surface properties of the resulting material upon successful intercalation of PA inside the Zn-Al LDH for the formation of an intercalated compound, we measured the surface area and pore size distribution using nitrogen gas adsorption-desorption technique at 77 K.

Figure 5 shows the adsorption-desorption isotherms for ZANIL and ZAPAN. As shown in the figure, the adsorption-desorption isotherm for ZAPAN is of type IV, indicating mesopores-type material (20–500 Å) [18], with adsorption increasing fairly rapidly at low relative pressure in the range of 0.0–0.05, followed by a slow uptake of the absorbent at a higher relative pressure of 0.5–0.6. Further increase of the relative pressure to > 0.6 resulted in a rapid adsorption of the adsorbent, reaching an optimum at more than 220 $cm^3/g$ at STP.

A general shape of the isotherm for ZAPAN does not differ very much from that of ZANIL, the type IV isotherm still remains. However, as shown in Fig. 5, the adsorbate uptake is slow in the relative pressure range of 0.0–0.9, after which rapid adsorption can be observed. An optimum uptake was only about 20 $cm^3/g$ at STP, indicating slow uptake of the nitrogen gas. The desorption branch of the hysteresis loop for ZAPAN is much narrower compared to ZANIL, indicating different pore texture of the resulting material.

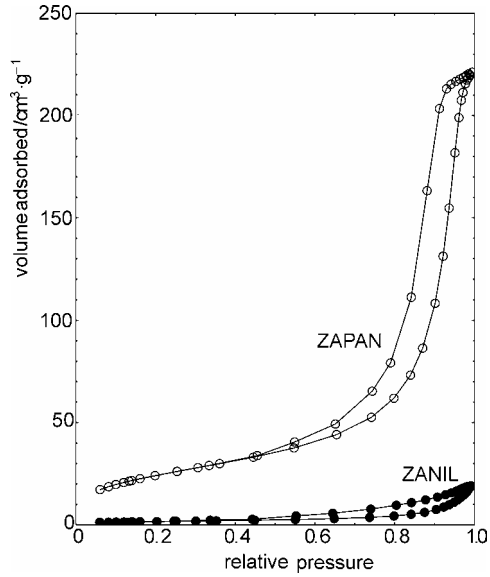


Fig. 5. Adsorption-desorption isotherms for ZANIL and ZAPAN

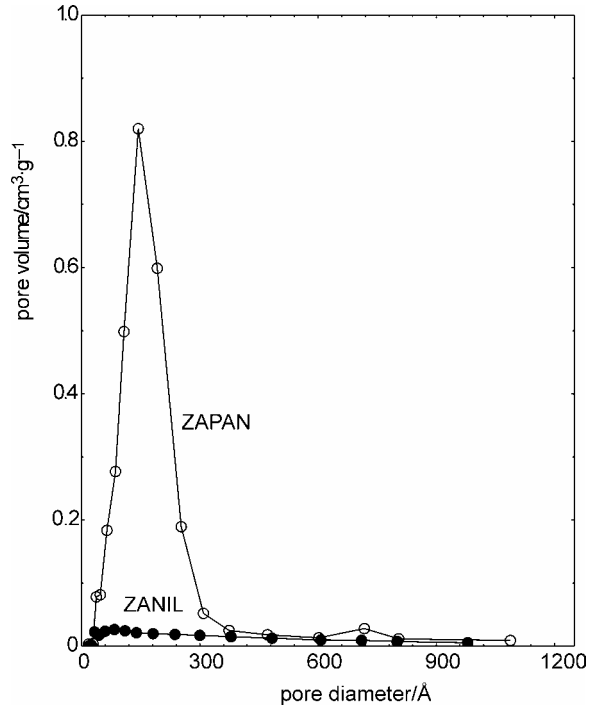


Fig. 6. BJH pore size distribution for ZANIL and ZAPAN

The surface properties of ZANIL and ZAPAN are summarised in the table. The intercalation of PA ion has increased the BET specific surface area from 6 $m^2/g$ for ZANIL to 90 $m^2/g$ for ZAPAN. The table shows that the BET average pore diameter for ZAPAN is lower than that of ZANIL, amounting to 149 Å and 173 Å, respec-

tively. On the other hand, the BJH desorption pore volume of ZAPAN is higher than that of ZANIL (0.342 to 0.028 $cm^3/g$, respectively).

The BJH pore size distribution for ZANIL and ZAPAN are presented in Fig. 6. Both materials show mesopores, in agreement with the adsorption isotherm of type IV. BJH pore size distribution for ZANIL shows a broad peak at around 100 Å while for ZAPAN an intense peak centred at around 145 Å is observed as well as another a very small, weak one at 700 Å, indicating modification of pore texture in agreement with the formation of a new intercalated compound with a basal spacing of 18 Å.

### 3.6. Surface morphology

Figures 7a and b show the morphology of ZANIL and ZAPAN obtained by an SEM. ZANIL and ZAPAN show typical morphology of LDH and its intercalated compound, which points to the existence of agglomerates of compact and non-porous granule structure.

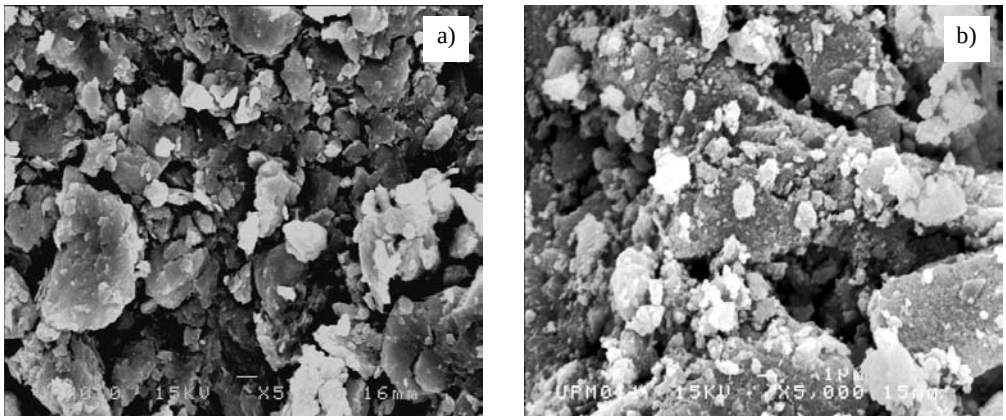


Fig. 7. Surface morphology for: a) ZANIL, b) ZAPAN

As shown in the figures, there is no significant difference in the morphology of the two samples. It is also very similar to the morphology of other intercalated compounds, such as Zn-Al-ibuprofen LDH, Mg-Al-poly(acrylic acid) LDH, Mg-Al -poly(vinylsulfonate) LDH and Mg-Al-poly(styrenesulfonate) LDH [2, 8].

## 4. Conclusion

Layered organic-inorganic intercalates can be prepared by using PA as a guest in Zn-Al LDH inorganic hosts by a self-assembly technique, with Zn:Al ratio of the mother liquor of 4:1. PXRD shows that the basal spacing of the Zn-Al LDH with nitrates as the intergallery anions expanded from 9 Å to 18 Å to accommodate the PA

anions for the formation of the Zn-Al LDH-PA layered inorganic-organic hybrid intercalated compounds. The FTIR study shows that the intercalated compound resembled the spectra of PA and ZANIL, indicating the presence of both functional groups in ZAPAN. It was also found that the BET surface area increases from 6 $m^2/g$ to 90 $m^2/g$ for the host (ZANIL) and the intercalated compound (ZAPAN), respectively, if 0.02 M PA is used for the synthesis of the latter. The pore texture of the resulting materials also changed as a result of the intercalation and the expansion of the basal spacing together with pore formation between the crystallite during the formation of the resulting layered intercalated compound. The morphologies of the LDH and its intercalated compound are quite similar, showing agglomerates and non-porous structures, the intercalation not very much influencing the morphology of the resulting intercalated compound.

**Acknowledgements**

We are grateful to the Malaysian Government for providing the grant under IRPA No. 09-02-0500-EA001. One of us (Z.J.) would like to thank Universiti Tenaga Nasional (UNITEN) for the scholarship.

## References

[1] MITZI D.B., *Synthesis, structure and properties of organic-inorganic perovskites and related materials*, Progress in Organic Chemistry, Wiley, New York, 1999, p. 1.
[2] ORIAKHI C.O., FARR I.V., LERNER M.M., J. Mater. Chem., 6 (1996), 103.
[3] WILSON O.C., OLORUNYOLEMI T., JAWORSKI A., BORUM L., YOUNG D., SIRIWAT A., DICKENS E., ORIAKHI C., LERNER M., Appl. Clay Sci., 15 (1999), 265.
[4] HUSSEIN M.Z., ZAINAL Z., YAHYA A.H., ABD AZIZ A., Mater. Sci. Eng. B 88 (2002), 98.
[5] YOU Y., VANCE G.F., ZHAO H., Appl. Clay Sci., 20 (2001), 13.
[6] HUSSEIN M.Z., HWA T.K., J. Nanoparticle Res., 2 (2000), 293.
[7] KUK W.K., HUH Y.D., J. Mater. Chem., **7** (1997), 1933.
[8] AMBROGI V., FARDELLA G., GRANDOLINI G., PERIOLI L., Inter. J. Pharma., 220 (2001), 23.
[9] ARCO M.D., RIVES V., TRUJILLANO R., J. Mater. Chem., 6 (1996), 1419.
[10] JORGENSEN M., J. Chromatogr. B: Biomedic. Sci. and Appl., 716 (1998), 315.
[11] MACKENSTEDT U., SCHMIDT S., MEHLHORN H., STOYE M., TRAEDER W., Parasitol. Res., 79 (1993), 567.
[12] MIYATA S., Clays Clay Miner., 13 (1983), 305.
[13] LEGROURI A., BADREDDINE A., BARROUG A., ROY J.P., BESSE P., J. Mater. Sci. Lett., 18 (1999), 1077.
[14] SILVERSTEIN R.M., BASSLER G.C., *Spectrometric Identification of Organic Compounds*, Wiley, New York, 1998.
[15] FERNANDEZ M., ULIBARRI M.A., LABAJOS F.M., RIVES V., J. Mater. Chem., 8 (1998), 2507.
[16] NIJS H., CLEARFIELD A., VANSANT E.F., Microporous and Mesoporous Materials, 23 (1998) , 97.
[17] VELU S., RAMKUMAR V., NARAYAN A., SWAMY C.S., J. Mater. Sci., 32 (1997), 957.
[18] SING K.S.W., *Characterization of Adsorbents*, Kluwer, Boston, 1989.

*Received 18 August 2003*
*Revised 29 October 2003*

*Materials Science-Poland, Vol. 22, No. 1, 2004*

# Synthesis, structure and magnetic susceptibility of ammonium hexaiodorhenate(IV)

ANDRZEJ KOCHEL*

Faculty of Chemistry, University of Wrocław, ul. Joliot-Curie 14, 50-383 Wrocław, Poland

This work reports on the synthesis, magnetic properties and crystal structure of $(NH_4)_2ReI_6$. Bright violet $(NH_4)_2ReI_6$ is tetragonal, *P4/mnc* (No. 128), $a = b = 7.7436(6)$, $c = 11.6403(14)$ Å, $Z = 2$, $D_x = 4.68$ g/cm$^3$, $T = 100(1)$ K. The structure was refined to $R = 0.074$ for 438 reflections observed. The anion $[ReI_6]^{2-}$ has an octahedral environment. The temperature dependence of the magnetic susceptibility measured over the range of 4–300 K exhibits the Curie point at 20 K, indicating the presence of antiferromagnetic interaction between the rhenium centres.

Keywords: *rhenium(IV); iodine complex; magnetic susceptibility*

## 1. Introduction

The magnetic susceptibilities of $K_2ReCl_6$ and $K_2ReBr_6$ have been measured over the temperature range of 80–300 K by several authors [1–4]. The effective magnetic moments calculated from the equation $\mu_{eff} = 2.84[\chi_m(T + \theta)]^{0.5}$ range from 3.6 to 3.8 B.M., compared to 3.87 B.M. for the spin-only moment of three unpaired electrons in the 5d shell. However, the magnetic moment of 3.87 B.M. should not be observed because of a relatively strong spin-orbit coupling exhibited by 5d transition ions. Rhenium salts with antiferromagnetic superexchange can be further used as starting materials for other antiferromagnetic materials. The replacement of $I^-$ ions in the $ReI_6^{2-}$ ion by other doubly (or more) binding ligands may lead to obtaining entirely new Re(IV) complexes with interesting magnetic properties.

The compound under study possesses interesting magnetic properties. In this salt, the occurrence of antiferromagnetic superexchange phenomenon is observed, and it might be useful for obtaining new Re(IV)-based magnetic substances.

*E-mail: andrzej@wchuwr.chem.uni.wroc.pl.

# 2. Experimental

## 2.1. Synthesis

$(NH_4)_2ReI_6$ was obtained by a reaction of $NH_4ReO_4$ with $NH_4I$ in an HI solution, as reported previously [5]. 10 g of ammonium tetraoxorhenate(IV) and 1.2 g of ammonium iodide were heated at 80 °C in 0.5 $dm^3$ of concentrated hydroiodic acid. The reaction stopped after 21 hours. A change of colour was observed during the reactions, from colourless to yellow, brown, dark brown and the final colour was black. The product was washed separately with $CHCl_3$ (about 2.5–3 $dm^3$ until the $CHCl_3$ was colourless) and ethyl ether. The elemental analyses of C, H and N matched the theoretical calculations. Preparation of crystals for X-ray measurements is very difficult and only very few of them were found appropriate for X-ray investigations.

## 2.2. Physical measurements

Magnetic measurements of polycrystalline samples were carried out over the temperature range of 4–300 K using a Quantum Design SQUID-Based Magnetometer MPMSXL5. The measurements were carried out at the Faculty of Chemistry, University of Wrocław, Wrocław, Poland. The SQUID magnetometer was calibrated with a palladium rod sample for which the gram susceptibility was assumed as $5.30\times10^{-6}$ $cm^3\cdot g^{-1}$ at 293 K (National Bureau of Standards, USA). The susceptibility measurements were made in the field of 0.5 T. Corrections were done for the diamagnetic response of the sample rod and of the sample using Pascal's constants [6].

Table 1. Crystallographic data and structure refinement details for $(NH_4)_2ReI_6$

| | | | |
|---|---|---|---|
| Empirical formula | $H_8N_2I_6Re$ | $F(000)$ | 830 |
| Formula weight | 983.68 | Crystal size | 0.07×0.05×0.05 mm |
| Temperature | 100(1) K | $\Theta$ range for data collection | 3.72–28.29 deg |
| Wavelength | 0.71073 Å | Index ranges | $-8 \le h \le 10$<br>$-9 \le k \le 10$<br>$-15 \le 1 \le 14$ |
| Crystal system | tetragonal | No. of reflections collected | 4213 |
| Space group | *P4/mnc* (No.128) | No. of independent reflections | 438 ($R$(int) = 0.0739) |
| Unit cell dimensions | $a = b = 7.7436(6)$ Å<br>$c = 11.6403(14)$ Å | Refinement method | full-matrix least-squares on $F^2$ |
| Volume | 697.99(11) $Å^3$ | Goodness-of-fit on $F^2$ | 1.05 |
| $Z$ | 2 | Final $R$ indices [$I > 2(I)$] | $R1 = 0.0739$, $wR2 = 0.1584$ |
| Density (calculated) | 4.68 $Mg/m^3$ | $R$ indices (all data) | $R1 = 0.0757$, $wR2 = 0.1589$ |
| Absorption coefficient | 9.91 $mm^{-1}$ | | |

A crystal of approximate dimensions of 0.07×0.05×0.05 $mm^3$ was used for the data collection. The intensity data were collected at 100(1)K using a CCD detector on

a KM4 diffractometer and graphite-monochromated MoKα radiation. The images were indexed, integrated, and scaled using the KUMA CrysAlis [7] data reduction package. The experimental details together with crystal data are given in Table 1. The structure was solved by heavy atom methods using SHELXS97 [8] and refined by least-squares minimization of $\sum w(F_0^2 - F_c^0)^2$ for all reflections [9]. The Re, I and N atoms were refined with anisotropic thermal parameters. The data were corrected for absorption [7]: $T_{min} = 0.789$ and $T_{max} = 0.967$.

## 3. Results and discussion

Diffraction measurements for powdered samples of $K_2ReI_6$ were performed by Morrow [10]. They indicated an orthorombic unit cell with $a$ = 11.07(5) Å, $b$ = 13.48(7) Å and $c$ = 10.19(5) Å, with four molecules in the unit cell. $(NH_4)_2ReI_6$ crystallizes in the tetragonal space group *P*4/*mnc* (No. 128), $a = b$ = 7.7436(6), $c$ = 11.6403(14) Å, $Z$ = 2, $D_x$ = 4.68 g/cm$^3$, $T$ = 100(1) K. The molecular structure and crystal packing of $(NH)_2ReI_6$ are shown in Figs. 1 and 2.

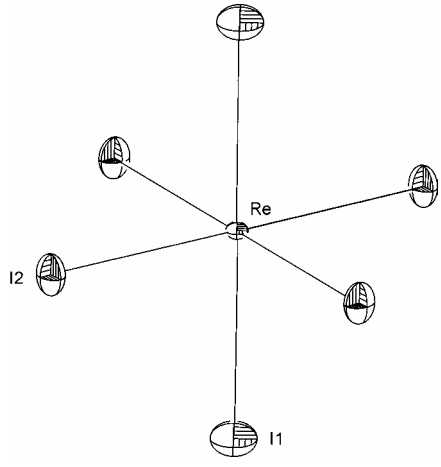


Fig. 1. The molecular structure of $(NH_4)_2ReI_6$

The atomic coordinates and equivalent displacement parameters are given in Table 2. The Re–I1 and Re–I2 bonds are 2.745(4) and 2.715(2) Å, respectively. The bond of 2.745(4) Å is longer and this fact is connected with a special position of the rhenium atoms. The bond lengths Re–I, found from the EXAFS study, were equal to 2.73 Å [11]. The Re–Re distances found in $K_2ReCl_6$ and $K_2ReBr_6$ are equal to 6.97 Å and 7.38 Å, the Re–X distances are 2.37 Å and 2.50 Å, and the shortest X–X contacts are 3.62 Å and 3.84 Å [12, 13]. In $(NH_4)_2ReI_6$ the shortest Re–Re distance is 7.74 Å, the Re–I equals 2.73 Å and the shortest contact between I–I in the crystal lattice equals 4.18 Å [Re–I1–I2 (–0.5 + $x$, –0.5 – $y$, –0.5 + $z$)].

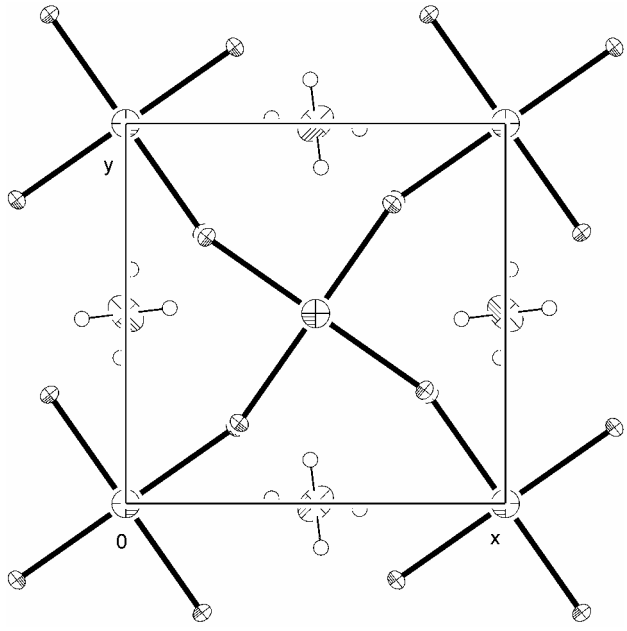


Fig. 2. The crystal packing of $(NH_4)_2ReI_6$ viewed along the [001] direction. The thermal ellipsoids are drawn at 30% probability

Magnetic properties of a series of iodocomplexes have been previously described in literature [14, 15], but the crystal structures were not reported. The effective magnetic moment ($\mu_{eff}$) of $(NH_4)_2ReI_6$ in the solid state is 3.00 B.M. at room temperature, which is consistent with a $d^3$ electronic configuration in an octahedral geometry. The effective moment 3.00 B.M. is reduced in comparison with the spin-only value (3.87) which can be due to a zero-field splitting and intermolecular interactions. The superexchange mechanism involves an interaction of electrons with opposite spins via intervening diamagnetic anions. This type of interaction has been frequently used to explain the antiferromagnetism of simple oxides and fluorides where metal ions are coupled by a single $O^{2-}$ or $F^-$ ion [16, 17]. In $(NH_4)_2ReI_6$, the rhenium centres are coupled by the $I^-$ ions, and in other hexachalogenorhenates by $Cl^-$ or $Br^-$ ions.

Table 2. Fractional atomic coordinates, equivalent isotropic displacement parameters $U_{eq}$ (in Å$^2$) with their e.s.d.'s (in parentheses) for $(NH_4)_2ReI_6$. $U_{eq}$ is defined as one third of the trace of the orthogonalized $U_{ij}$ tensor

| Atom | $x$ | $y$ | $z$ | $U_{eq}/U_{iso}$ |
|---|---|---|---|---|
| Re | 0 | 0 | 0.5 | 0.0067(6) |
| I1 | 0 | 0 | 0.2642(3) | 0.0289(9) |
| I2 | 0.2010(3) | –0.2872(3) | 0.5 | 0.0195(6) |
| N | 0 | –0.5 | 0.25 | 0.042(14) |
| H | 0.01(4) | –0.383(13) | 0.28(2) | 0.02(7) |

This superexchange path, e.g. with two intervening $I^-$ ions, takes the following form

$$Re - I \cdots I - Re$$

The magnetic susceptibility ( $\chi_m$) was measured from 4 to 300 K and indicated one strong maximum ($T_{Néel}$) at 20 K. Below 8 K, the magnetic susceptibility data suggest existence of another phase.

The magnetic properties are shown in Fig. 3 in the form of $\chi_m$ vs. $T$ and $\mu_{eff}$ vs. $T$. From 10 to 20 K (20 K, $T_{Néel}$) we observe antiferromagnetic interactions, then paramagnetic ones, but the most interesting are susceptibilities from 10 K to 4 K.

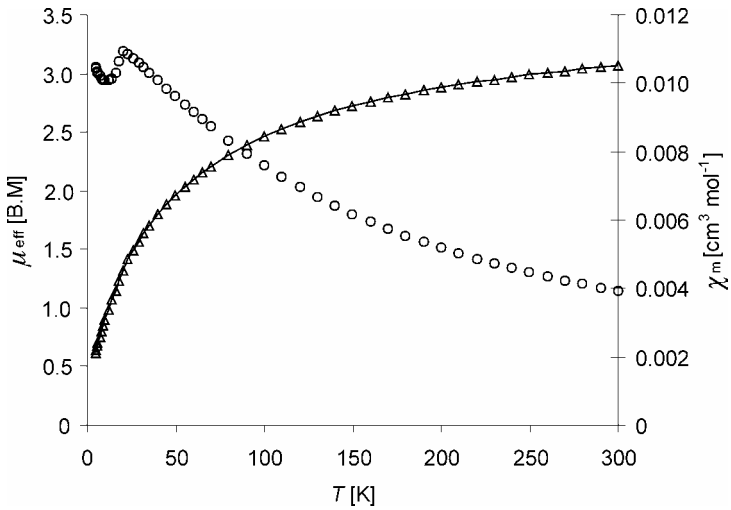


Fig. 3. Plots of $\chi_m$ vs. $T$ (o) and $\mu_{eff}$ vs. $T$ (Δ) for $(NH_4)_2ReI_6$. The solid line represents the best fit to the experimental data

In this region, the susceptibility runs into another maximum which suggests another phase of ferromagnetic interactions. Unfortunately, an answer will not be possible until a neutron diffraction study or X-ray measurements at the temperature of liquid He is performed. The presence of $T_{Néel}$ and a strong decrease of the magnetic moment below 200 K and an accompanying change of $\chi_m$ suggest the presence of an antiferromagnetic coupling between the rhenium(IV) centres, clearly bridged by the $I^-$ ions. The magnetic susceptibility data are analyzed using the classical spin Hamiltionian [18]:

$$H = 2D\left[S_Z^2 - \frac{1}{3}S(S+1) + g_{\parallel}\beta H_z S_z + g_{\perp}\beta(H_x S_x + H_y S_y)\right] \quad (1)$$

The experimental magnetic data for $(NH)_2ReI_6$ were fitted to the empirical relations proposed earlier [19]

$$\chi_{\parallel} \frac{N\beta^2 g_{\parallel}^2}{4kT} \frac{1+9\exp\left(-\frac{2D}{kT}\right)}{1+\exp\left(-\frac{2D}{kT}\right)}$$

$$\chi_{\perp} = \frac{N\beta^2 g_{\perp}^2}{4kT} \frac{4+6\left(\frac{kT}{2D}\right)\times\left[1+\exp\left(\frac{-2D}{kT}\right)\right]}{1+\exp\left(\frac{-2D}{kT}\right)}$$

where: $D$ is the zero-field splitting, $N$ – Avogadro's number, $g$ – the spectroscopic splitting factor, $\beta$ – the Bohr magneton, $k$ – the Boltzmann constant and $T$ – the absolute temperature. Since our data concern powdered samples, the experimental magnetic susceptibility $\chi_{av}$ equals $(1/3\chi_{\parallel} + 2/3\chi_{\perp})$. The best fit parameters were obtained by minimizing the function

$$R = \left[\frac{\sum_{i=1}^{n}\left(\chi_m^{exp} - \chi_m^{calc}\right)^2}{\sum_{i=1}^{n}\left(\chi_m^{exp}\right)^2}\right]^{0.5}$$

The parameters giving the best-fit were obtained using nonlinear regression analysis with $g = 1.93$; $2D = 6.52$ cm$^{-1}$and $R = 5.12\times10^{-3}$. The magnetic measurements suggest the presence of an antiferromagnetic superexchange interaction at the temperature between 10 and 20 K. At the moment we are unable to explain the temperature dependence of the magnetic susceptibility at low temperatures, from 10 K to 4 K. In $(NH_4)_2ReI_6$ we observed a stronger superexchange than in $K_2ReCl_6$ and $K_2ReBr_6$. It is possible that as the electronegativity of the anion decreases, the superexchange increases respectively. Thus, iodide rhenium salts should have stronger superexchange interaction than the chloride and bromide salts.

The antiferromagnetic effect observed is strongly influenced by the crystal structure alone. The symmetry of the $ReI_6^{2-}$ ions and the highly symmetric system into which the compound discussed crystallizes may be connected with a possibility of an antiparalled arrangement of the spins. Rhenium centres, where the central atom itself is already in an octahedral environment, arrange in the cell along particular directions in layers, directly influencing the ordering of the spins located at the $Re^{4+}$ ions. The thermal contraction also positively influences the strength of interactions between the centres which depend strongly on the Re–Re distances. The reduction of volume causes a reduction of the $I^-$–$I^-$ distances that play a key role in the compound discussed.

## Conclusions

The rhenium(IV) salts present antiferromagnetic superexchange interactions between rhenium centres during the $I^-$–$I^-$ contacts. $T_{Néel}$ for $(NH_4)_2ReI_6$ is 20 K. These salts can be starting materials for other iodocompounds because the $I^-$ ligands are more labile than $Br^-$ or $Cl^-$ ones. However, their synthesis and crystal growth are very difficult*.

## References

[1] NELSON C.M., BOYD G.E., SMITH W.Y., J. Am. Chem. Soc., 76 (1954), 348.
[2] FIGGIS B.N., LEWIS J., NYHLOM R.S., PEACKOK R.D., Disc. Faraday Soc., 26 (1959), 103.
[3] PERAKIS N., Compt. Rend., 206 (1938), 1369.
[4] SCHUTH W., KLEMM W., Z. Anorg. u. Allgem. Chem., 220 (1934), 193.
[5] *Inorganic Synthesis*, Vol. 7, J. Kleinberg (Ed.), McGraw Hill, New York, 1963, p. 191.
[6] KOENIG E., *Magnetic Properties of Coordination and Organometallic Transition Metal Compounds*, Springer-Verlag, Berlin, 1996.
[7] CrysAlis CCD, RED 166, Oxford Diffraction, Wrocław (Poland).
[8] SHEDRICK G.M., *SHELXS97, Program for Solution of Crystal Structure*, University of Goettingen, Germany, 1997; http://shelx.uni-ac.gwdg.de/SHELX/index.html.
[9] SHELDRICK G.M., *SHELXL97, Program for Refinement of Crystal Structure*, University of Goettingen, Germany, 1997; http://shelx.uni-ac.gwdg.de/SHELX/index.html.
[10] MOROW J.C., J. Chem. Soc., 60 (1956), 19.
[11] TOMKIEWICZ A., VILLAIN F., MROZŃSKI J., J. Mol. Struct., 555 (2000), 383.
[12] GRUNDY H.D., BROWN I.D., Canadian J. Chem., 48 (1970), 1151.
[13] TEMPLETON D.H., DAUBEN C.H., J. Am. Chem. Soc., 73 (1951), 4492.
[14] COLTON R., *The Chemistry of Rhenium and Technetium*, Wiley, New York, 1965.
[15] BENNET M.J., COTTON F.A., FOXMANN B.M., Inorg. Chem., 7 (1968), 1563.
[16] ANDERSON P.W.,Phys. Rev., 350 (1950), 79; 2 (1959), 115.
[17] KRAMERS H.A., Physica, 1 (1934), 182.
[18] FOGGIS B.N., Trans. Faraday Soc., 56 (1960), 1553.
[19] KAHN O., *Molecular Magnetism*, VCH, Weinheim, 1993.

*Received 7 March 2003*
*Revised 7 September 2003*

---

*Further details of the investigation of the crystal structure can be obtained from the Fachinformationszentrum Karlsruhe, 76344 Eggenstein-Leopoldshafen, Germany (fax(+49)7247-808-666; e-mail: crysdata@fiz.karlsruhe.de) on quoting depository number CSD-412940.